Journal of Medicinal Chemistry

pubs.acs.org/jmc

Article

Multitarget, Selective Compound Design Yields Potent Inhibitors of a Kinetoplastid Pteridine Reductase 1

Ina Pöhner,[§§] Antonio Quotadamo,[§§] Joanna Panecka-Hofman, Rosaria Luciani, Matteo Santucci, Pasquale Linciano, Giacomo Landi, Flavio Di Pisa, Lucia Dello Iacono, Cecilia Pozzi, Stefano Mangani, Sheraz Gul, Gesa Witt, Bernhard Ellinger, Maria Kuzikov, Nuno Santarem, Anabela Cordeiro-da-Silva, Maria P. Costi,* Alberto Venturelli,* and Rebecca C. Wade*

Cite This: *J. Med. Chem.* 2022, 65, 9011−9033

Read Online

ACCESS | Metrics & More | Article Recommendations | Supporting Information

ABSTRACT: The optimization of compounds with multiple targets is a difficult multidimensional problem in the drug discovery cycle. Here, we present a systematic, multidisciplinary approach to the development of selective antiparasitic compounds. Computational fragment-based design of novel pteridine derivatives along with iterations of crystallographic structure determination allowed for the derivation of a structure−activity relationship for multitarget inhibition. The approach yielded compounds showing apparent picomolar inhibition of *T. brucei* pteridine reductase 1 (PTR1), nanomolar inhibition of *L. major* PTR1, and selective submicromolar inhibition of parasite dihydrofolate reductase (DHFR) versus human DHFR. Moreover, by combining design for polypharmacology with a property-based on-parasite optimization, we found three compounds that exhibited micromolar EC_{50} values against *T. brucei brucei* while retaining their target inhibition. Our results provide a basis for the further development of pteridine-based compounds, and we expect our multitarget approach to be generally applicable to the design and optimization of anti-infective agents.

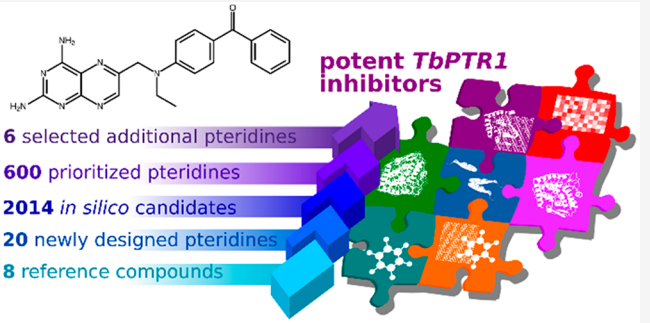

INTRODUCTION

The World Health Organization has identified 17 neglected tropical diseases (NTDs) that pose a health burden to over 1.4 billion people.[1,2] Parasites of the trypanosomatid family are responsible for two potentially lethal insect-vector borne NTDs: human African trypanosomiasis (HAT, sleeping sickness), caused by *Trypanosoma brucei*, and leishmaniasis, caused by the intracellular parasite *Leishmania spp.*[3−7] Current therapeutics are limited by toxicity, poor efficacy, and parasite resistance, thus underlining the need for new chemotherapies.[8,9]

New antiparasitic agents can be identified by target-based drug design strategies.[10−12] The folate pathway enzyme dihydrofolate reductase (DHFR) is a known anticancer, antibacterial, and antimalarial target.[13−16] It provides reduced folates, which are crucial to biological processes like DNA, protein, and amino acid synthesis or one-carbon transfer.[14,17,18] In trypanosomatids, DHFR inhibition, for example by methotrexate (MTX, **1a**), is ineffective due to a metabolic bypass via the biopterin-reducing pteridine reductase 1 (PTR1, Figure 1): when DHFR is inhibited, PTR1 is overexpressed and sustains sufficient reduced folate levels to ensure parasite survival. Thus, when targeting the folate pathway in *Leishmania*, both DHFR and PTR1 need to be considered.[19−21] In *T. brucei*, RNA interference studies have suggested PTR1 to be a potential antiparasitic target in its own right.[22,23] Nonetheless, even nanomolar PTR1 inhibitors have so far shown limited antiparasitic activity *in vitro*,[24,25] suggesting that targeting the *T. brucei* folate pathway may also benefit from the consideration of both PTR1 and DHFR.

Screening a set of folate-related compounds against parasitic folate pathway targets previously led to the identification of compounds **1b** (methyl-1-(4-(((2,4-diaminopteridin-6-yl)methyl)(methyl)amino)benzoyl)piperidine-4-carboxylate) and **1c** (methyl-1-(4-(((2,4-diaminopteridin-6-yl)methyl)amino)benzoyl)piperidine-4-carboxylate) as submicromolar inhibitors of *Leishmania major* PTR1 (*Lm*PTR1) with K_i values of 0.04 and 0.10 μM, respectively.[26] **1c** was additionally a micromolar inhibitor of *L. major* DHFR (*Lm*DHFR) with a weak selectivity for the parasite enzyme over the human DHFR (hDHFR) (K_i of 4 vs 10 μM). In contrast to the parasite DHFR, which is

Received: February 9, 2022
Published: June 8, 2022

Downloaded via UNIV DEGLI STUDI DI MODENA on February 1, 2023 at 10:58:04 (UTC).
See https://pubs.acs.org/sharingguidelines for options on how to legitimately share published articles.

ACS Publications

© 2022 The Authors. Published by American Chemical Society

https://doi.org/10.1021/acs.jmedchem.2c00232
J. Med. Chem. 2022, 65, 9011−9033

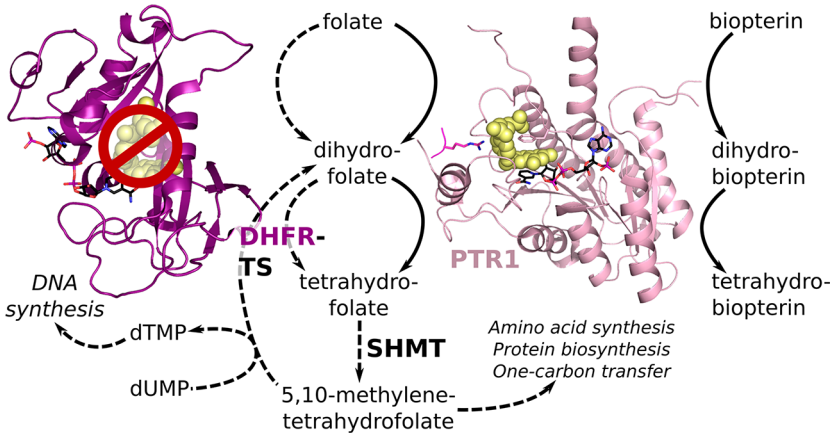

Figure 1. Overview of pterin activation in the trypanosomatidic folate pathway when DHFR is inhibited and PTR1 provides a metabolic bypass. Under normal conditions (indicated by dashed lines), the DHFR domain of the bifunctional DHFR-TS reduces biological folates to tetrahydrofolate (THF). Serine hydroxymethyl transferase (SHMT) converts THF to 5,10-methylene THF, which has a central role in amino acid synthesis, protein biosynthesis, and one-carbon transfer. It is also required by the TS domain of DHFR-TS to convert deoxyuridine monophosphate (dUMP) to deoxythymidine monophosphate (dTMP), which is necessary for DNA synthesis. PTR1 catalyzes the reduction of unconjugated pterins, like biopterin, and takes over folate reduction when DHFR is inhibited (continuous lines), thus acting as a metabolic bypass and an important additional target for shutting down the trypanosomatidic folate pathway. Both proteins are shown in cartoon representation (DHFR domain of DHFR-TS: purple, PTR1 monomer of the functional tetramer: light pink) with the NADPH/$NADP^+$ cofactor in a stick representation with black carbons and the folate substrate in yellow spheres. In PTR1, an arginine residue from a neighboring subunit that points into the active site is shown in a magenta stick representation.

covalently coupled with thymidylate synthase (TS) in a bifunctional DHFR-TS, the hDHFR off-target is monofunctional and shares only about 30% sequence identity with parasite DHFR domains, indicating potential for further optimization of selectivity.[27−29]

The current study focuses on optimizing pteridine-based compounds for their inhibition of *T. brucei* PTR1 (*Tb*PTR1) and *Tb*DHFR, in addition to the corresponding *Leishmania* targets, while ensuring selectivity against the off-target hDHFR. The enzymatic evaluation of reference pteridines reported earlier,[26,30] our comparative study of trypanosomatid folate pathway proteins,[31] and computational docking studies were first employed for the design of novel pteridine derivatives. Three new crystal structures of complexes of pteridines with *Tb*PTR1 and a complex with *Lm*PTR1 were determined and confirmed the predicted bound orientation of the novel pteridines. A systematic analysis of correlations between computed physicochemical molecular descriptors and observed antiparasitic effects was then performed and allowed us to prioritize promising compounds for synthesis. In total, we identified 26 new pteridine-based multitarget inhibitors showing improved target inhibitory profiles for PTR1 and DHFR of both *L. major* and *T. brucei*. Among these inhibitors, we report the first, to the best of our knowledge, apparent picomolar inhibitors of *Tb*PTR1 and several new low nanomolar inhibitors of *Lm*PTR1, which mostly also show selective micromolar to submicromolar inhibition of the parasite DHFR variants. *In vitro* evaluations of the designed multitarget inhibitors against bloodstream forms of *T. brucei brucei* revealed low micromolar to submicromolar EC_{50} values for three of these pteridines. Taken together, we here report a successful application of a systematic multitarget design approach to yield selective pteridine-based antiparasitic compounds affecting multiple trypanosomatid enzymes.

RESULTS AND DISCUSSION

Reference Compounds Inhibit both PTR1 and DHFR. To systematically assess multitarget inhibition, we measured the inhibition of *Tb*PTR1, *Tb*DHFR, *Lm*PTR1, *Lm*DHFR, and the off-targets hDHFR and hTS by the folate-related anticancer agent methotrexate (MTX, **1a**) and seven further pteridine-based reference compounds (**1b**−**1h**, Figure 2 and Table S1, SI).[26,30,32] Although **1b**−**1h** were primarily designed as *Lm*PTR1 inhibitors, we found all to be more potent against *Tb*PTR1 than *Lm*PTR1 with **1b** being the strongest inhibitor of *Tb*PTR1 with an IC_{50} of 50 nM against *Tb*PTR1 and 1 μM against *Lm*PTR1 (Figure 2A). Notably, these compounds exhibited micromolar to submicromolar inhibition of *Lm*DHFR and *Tb*DHFR (IC_{50} *Lm*DHFR 0.3−1.4 μM; *Tb*DHFR 0.3−20.05 μM). While MTX (**1a**) was more potent against the parasite DHFRs, it was not selective (selectivity index SI: *Tb*DHFR/hDHFR = 3 and *Lm*DHFR/hDHFR = 1, Figure 2A). For compounds **1b**−**1h**, higher SI values were observed, ranging up to about 165 for **1b** for both *Tb*DHFR and *Lm*DHFR (Figure 2A).

Substrate-like and Methotrexate-Inhibitor-like Binding Modes of the Reference Compounds. Despite the hydrogen-bonding network stabilizing the pteridine ring in the PTR1 active site, for the PTR1 complexes with MTX/**1a** derivatives, there are two alternative binding modes. Previously determined crystal structures show that compounds **1b** and **1c** share a substrate-like pterin orientation in the complex with *Lm*PTR1.[26] In the same crystal structure, compound **1b** also adopts a second, so-called inhibitor-like (or MTX-like) orientation, with the bicyclic ring system flipped by 180° and rotated by 30° (Figures 3A,B and S1).[26] Dual binding modes have also been observed in crystallographic complexes of *Tb*PTR1 with small pteridine-based inhibitors.[32]

We here determined the crystal structure of the ternary complex of *Tb*PTR1 with NADPH/$NADP^+$ and the reference compound **1b** (PDB-ID 6rx5, resolution 1.42 Å, experimental details: Tables S2 and S3). It shows that the diaminopteridinyl

https://doi.org/10.1021/acs.jmedchem.2c00232
J. Med. Chem. 2022, 65, 9011−9033

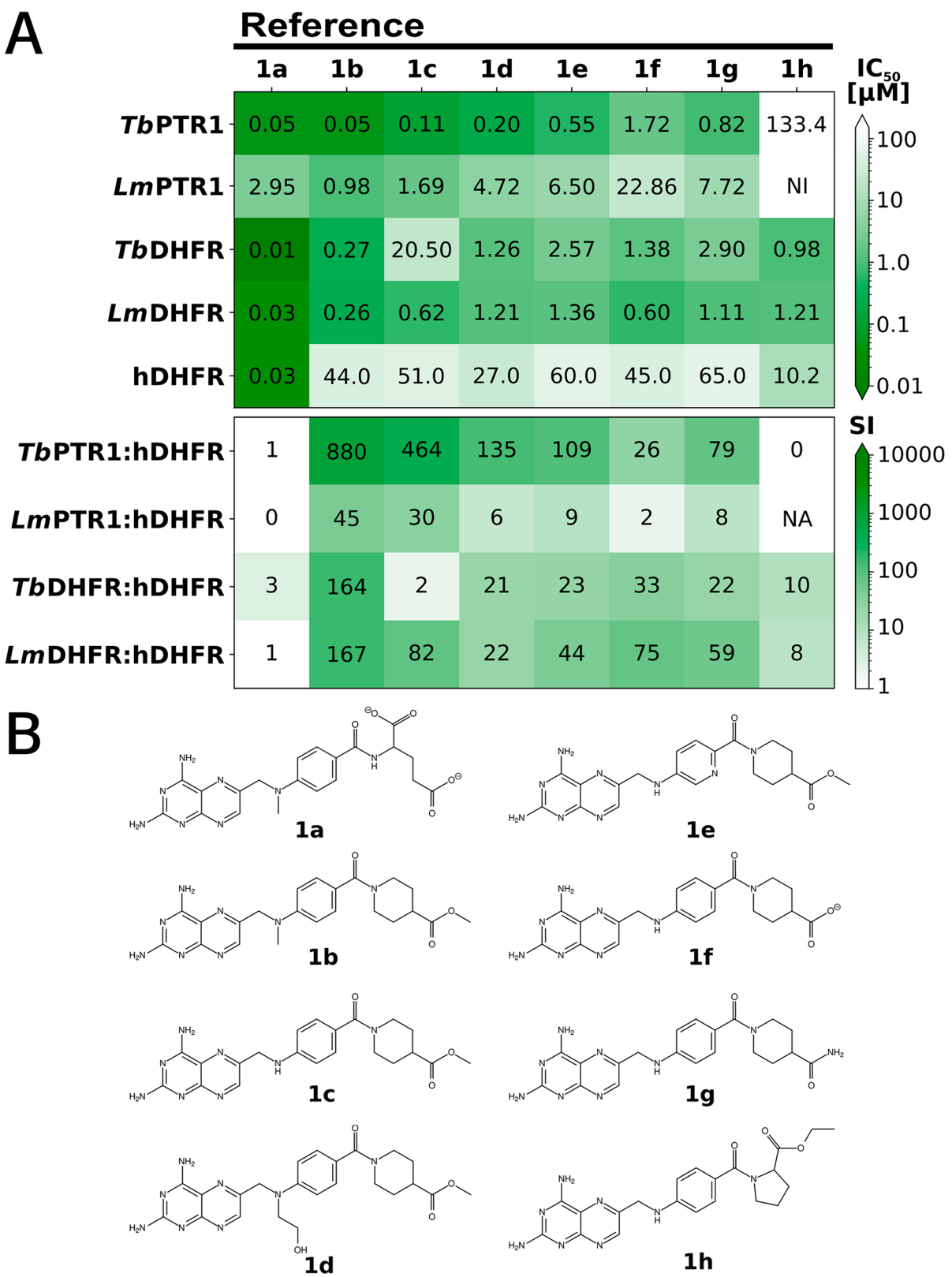

Figure 2. Inhibitory activities, selectivities, and structures of reference pteridines. (A) Heatmaps show activities given by IC_{50} values (top) and selectivity indices (SI) (bottom) for the targets and the off-target hDHFR. All values, as well as data for hTS, are given in Table S1. NI: no inhibition; NA: not applicable. (B) Previously published compounds shown were used as reference compounds: **1a** is methotrexate; **1b**, **1c**, and **1h** are **6b**, **6a**, and **6c** from Cavazzuti et al.;[26] and **1d**−**1g** correspond to **5d**, **5b**, **6a**, and **5a** from Corona et al.[30]

moiety of **1b** adopts only the MTX-like orientation (Figure 3C), resembling its MTX-like binding mode in *Lm*PTR1 (Figures 3B and S2). Consistently, docking studies indicated that all reference pteridines adopt MTX-like binding modes in the different targets and the off-target hDHFR (Table S4 and Figure S5). Therefore, we concluded that the MTX-like binding mode

https://doi.org/10.1021/acs.jmedchem.2c00232
J. Med. Chem. 2022, 65, 9011−9033

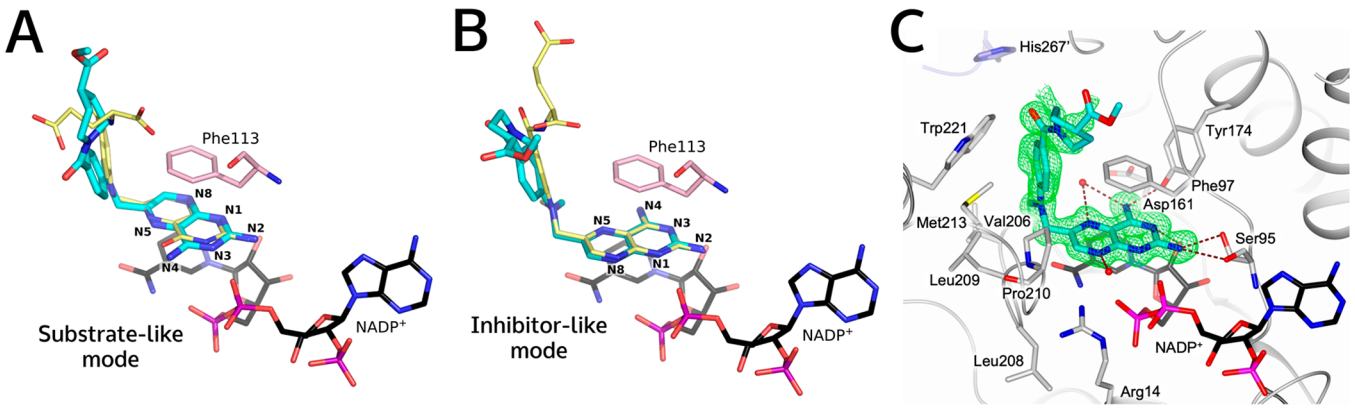

Figure 3. Orientations of reference pteridine compound **1b** in crystal structures of *Lm*PTR1 and *Tb*PTR1. (A,B) Compound **1b** (cyan carbons) in complex with *Lm*PTR1 (PDB-ID 2qhx) has a substrate-like (A) and an inhibitor-like or MTX-like (B) binding mode. **1b** is shown with (A) folate (yellow carbons) superimposed from a *Tb*PTR1 structure (PDB-ID 3bmc) and with (B) MTX (**1a**, yellow carbons) superimposed from an *Lm*PTR1 structure (PDB-ID 1e7w). The pteridine nitrogens are labeled according to the ring nomenclature. (C) Binding site in the crystal structure determined in this work (PDB-ID 6rx5) of *Tb*PTR1 (gray cartoon, His267′ from the neighboring subunit in lavender) in complex with NADPH/$NADP^+$ and compound **1b**, which has the MTX-like binding mode. Interacting residues (in A, B: only Phe113) and the NADPH/$NADP^+$ cofactor are shown in sticks (carbons colored according to protein and black, respectively). In (C), water molecules are shown as red spheres, and the inhibitor is surrounded by the omit map (green wire) contoured at the 2.5 σ level. Hydrogen bonds are represented by brown dashed lines.

is likely the dominant one, and we focused on the analysis of this binding mode in the subsequent compound design.

Comparative Target/Off-Target Mapping and Docking Studies Support Design Focused on Selective Multitarget Inhibition. To develop enhanced selective inhibitors of the parasite targets, we employed a multitarget-based design approach to improve inhibition of *Tb*PTR1, *Tb*DHFR, *Lm*PTR1, and *Lm*DHFR while retaining low hDHFR off-target inhibition. The next generation of pteridine-like compounds was created by dissecting the part of **1b** attached to the pteridine core into three modules. These were N10, the substitution to the N10 position; PABA, the *para*-amino benzoic acid (PABA) moiety; and Tail, the cyclic glutamate tail (Figure 4). We separately modified each of these modules to obtain three new series of compounds. The modifications of each module were based on binding mode predictions from docking in the different targets and the off-target hDHFR and our previously published optimization guidelines for MTX-like scaffolds.[31] The key concepts adopted in the compound design are summarized in Figure 4.

Rationale for N10 Modifications. The binding pockets of the different target proteins were found to share a number of aliphatic residues in the proximity of the N10 substituent of a bound ligand, e.g., Leu209 of *Tb*PTR1; Ile47 and Leu90 of *Tb*DHFR; Leu226 and Leu229 of *Lm*PTR1; Ile20 and Val62 of *Lm*DHFR (Figure 4A).[31] Bulkier nonpolar groups in comparison to the methyl of **1b**, like the ethyl and propargyl substituents of **2a** and **2b**, allow for interactions with those hydrophobic moieties. Docking studies suggested that even substituents of the size of benzyl, as in **2c**, can be accommodated in the PTR1 and DHFR pockets (Figure 5A,B). Furthermore, such bulky substituents may improve selectivity for the on-targets: The hDHFR pocket has a lower volume compared to the parasite DHFR pockets (pocket volume *Tb*DHFR 353 $Å^3$, *Lm*DHFR 384 $Å^3$, and hDHFR 347 $Å^3$).

Furthermore, as previously demonstrated,[31] hDHFR favors hydrogen bond donors in the proximity of N10 and the PABA ring system, whereas the parasite DHFRs allow for favorable interactions with hydrogen bond acceptors. To improve off-target selectivity, we thus replaced N10 by sulfur and the PABA benzene ring by pyridine in **2d**.

Although Corona et al.[30] found improved selectivity for PTR1 over hDHFR by hydrophilic N10 substitutions, our data for reference compound **1d** with a hydroxyethyl substituent did not support this observation (Figure 2A). Docking simulations indicated that interactions with a highly conserved structural water might induce an unfavorable conformation of the substituent's aliphatic chain (Figure S5A, SI). To relax the geometry while allowing interactions between the substituent and water, we elongated the aliphatic linkage to a hydroxypropyl in **2e**.

Thus, in total, the N10 series consists of five novel pteridines (**2a**–**e**, Figure 6) modified to improve interactions with PTR1 and parasite DHFR and to exploit the differences in pocket sizes and residues between the parasitic targets and the hDHFR off-target.

Rationale for PABA Modifications. As a first modification to the PABA moiety, in **3a**, we replaced the PABA phenyl group with benzyl (Figure 6). The additional hydrophobic spacer can interact with hydrophobic target residues while resulting in a shifted position of the hydrophilic linker amide. The positioning of hydrophobic and hydrophilic residues surrounding the PABA moiety and the amide linker in the human off-target is different from that of the parasite targets PTR1 and DHFR, which can be exploited to improve selectivity. For the same reason, the amide linker position was also shifted in **3b** by substituting the PABA moiety with *meta*-aminobenzoic acid.

A second key feature of the targets vs off-targets that was used to inform the design of the PABA series relates to the compound tail: Tail regions are solvent-exposed in PTR1 and thus have poorly defined interactions (Figure 4B). In contrast, in DHFR, the tail region is enclosed, and strong interactions occur with the hDHFR off-target.[31] We therefore shortened the tail region to achieve full enclosure in the PTR1 binding pocket by replacing PABA by naphthalene (**3c**) or benzene moieties (non-substituted, **3d**; or substituted with $-CF_3$, **3e**). Docking results showed that the smaller tail fully resides in the PTR1 binding pocket (Figure 5C) and is stabilized by surrounding hydrophobic residues, not only in PTR1 but also in parasite DHFR

https://doi.org/10.1021/acs.jmedchem.2c00232
J. Med. Chem. 2022, 65, 9011−9033

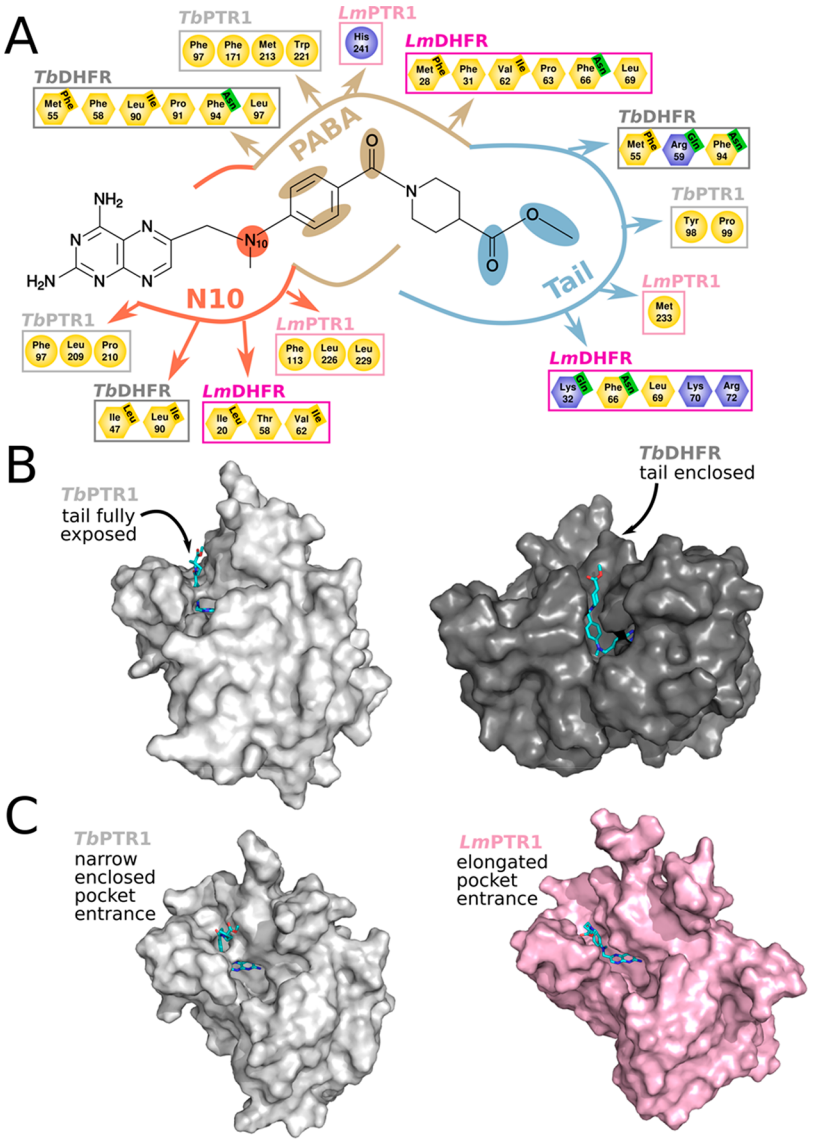

Figure 4. Structural features of PTR1 and DHFR considered in the multitarget design of selective compounds illustrated for reference compound **1b**. (A) Selected residues within 5 Å of the three modules—N10, PABA and Tail—modified in the design procedure. Residues were selected for the complexes of **1b** with *Tb*PTR1 (pale gray), *Tb*DHFR (dark gray), *Lm*PTR1 (pale pink), and *Lm*DHFR (dark pink). Residues are colored according to their properties: basic: blue, polar: green, and nonpolar: yellow. The ligand interaction plot is based on Panecka-Hofman et al.[31] and provides an overview of residues with similar properties that surround the ligand modules in the different targets (showing only those applied for the design; for full maps, see Figures S3 and S4). In some positions, the amino acid type of the off-target hDHFR is different from parasite DHFR. Differing hDHFR residues are labeled in the top right corner of the corresponding parasite DHFR residue. These positions highlight suitable substitution points to improve selectivity. (B) Surface representations of complexes of **1b** with *Tb*PTR1 (left, PDB-ID 6rx5) and *Tb*DHFR (right, MTX-like top-ranked docking pose in PDB-ID 3rg9). The compound tail moiety is fully solvent-exposed in PTR1, whereas it is well-enclosed in DHFR. (C) Surface representations of complexes of **1b** with *Tb*PTR1 (left, PDB-ID 6rx5) and *Lm*PTR1 (right, PDB-ID 2qhx, state A). The ligand is more enclosed in the narrow pocket entrance of *Tb*PTR1, while the *Lm*PTR1 pocket has an elongated, widened funnel that can accommodate larger compound tails. In (B,C), **1b** is shown in sticks with cyan carbons.

(Figure 5C,D). Rigid-body docking studies suggested that the bulky naphthalene of **3c** may be particularly beneficial in *Lm*PTR1, since this target has a more elongated, open pocket compared to *Tb*PTR1 (Figure 4C). The PABA moiety modifications are therefore suitable for modulating the compound interaction profile in a species-specific manner.

In summary, the PABA series contains five new pteridine derivatives (**3a**−**3e**, Figure 6) designed to improve selectivity by exploiting the different surroundings of bound PABA moieties in hDHFR in comparison to the parasite target proteins.

Rationale for Tail Modifications. The surrounding of the compound tail features several hydrophobic residues, particularly in the two *T. brucei* targets (Figure 4A). Directional interactions with the tail moiety may have limited benefit for the binding affinity in PTR1, since the flexibility of the solvent-exposed tail likely has an entropic contribution. Hydrophobic interactions are geometrically less restrained than, for instance, hydrogen bonds. Therefore, anticipating less pronounced entropic penalties on binding in our designed derivatives, we replaced the methyl ester in the tail of **1b** by the more flexible ethyl and propyl in **4a** and **4b**, respectively. Two aspects may

https://doi.org/10.1021/acs.jmedchem.2c00232
J. Med. Chem. 2022, 65, 9011−9033

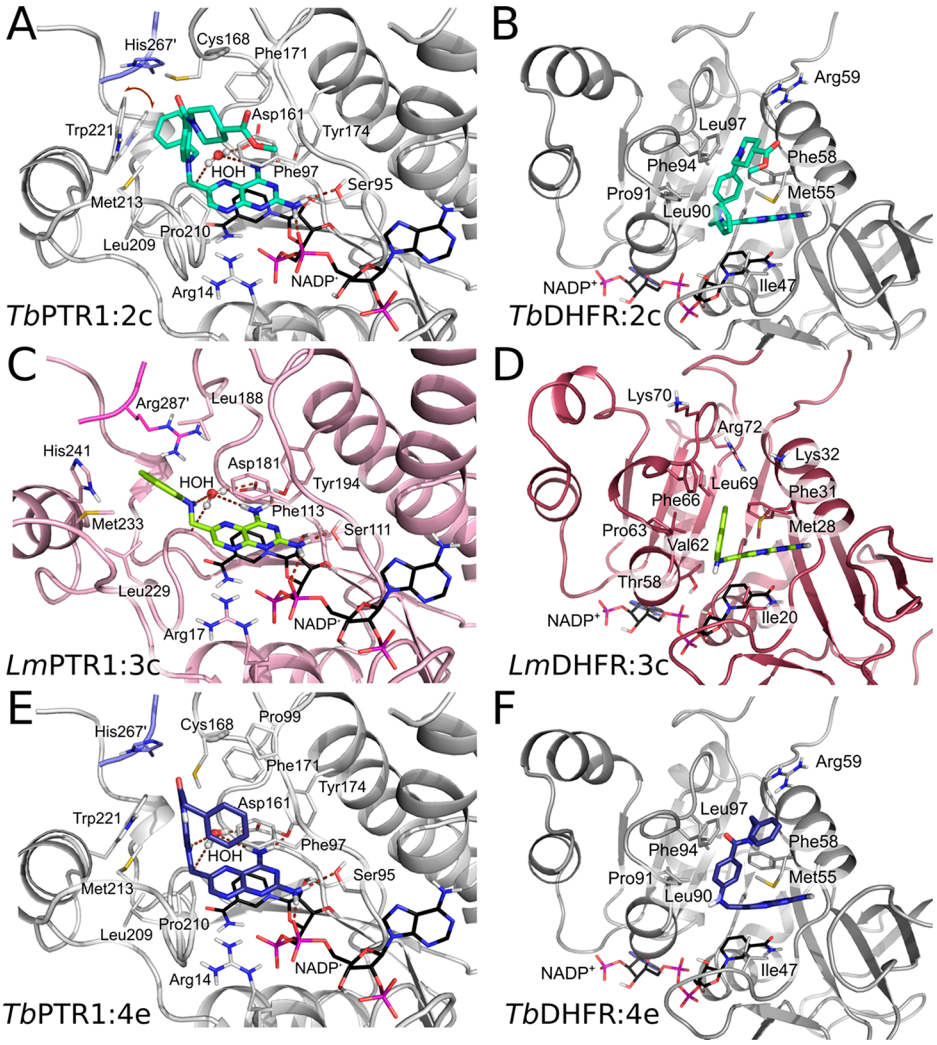

Figure 5. Views of the binding sites showing docked poses of selected pteridine-based inhibitors in the target proteins: *Tb*PTR1 (pale gray) (A,E), *Tb*DHFR (dark gray) (B,F), *Lm*PTR1 (pale pink) (C), and *Lm*DHFR (dark pink) (D). (A) Induced fit (IF) MTX-like docking pose for compound **2c** (cyan carbons) in *Tb*PTR1 in the presence of a conserved water molecule (ball-and-stick representation): Trp221 moves (indicated by a brown arrow) to make room for the phenyl of **2c**. (B−F) Rigid-body docking poses of **2c** in *Tb*DHFR (B), **3c** (lime carbons) in *Lm*PTR1 and *Lm*DHFR (C,D), and **4e** (purple carbons) in *Tb*PTR1 and *Tb*DHFR (E,F); see text for discussion. Docked poses are shown for N1-deprotonated compounds, but similar orientations were observed for the N1-protonated forms (see Figure S6). For PTR1, all docking poses shown were obtained in the presence of conserved structural water molecules. Generally, similar poses were observed for docking without water. In all panels, proteins are shown in cartoon representation with the important interacting residues (compare Figure 4A) and the NADPH/$NADP^+$ cofactor shown in sticks (carbons colored according to protein and black, respectively). Residues His267′ and Arg287′ from the neighboring subunit are shown in lavender and magenta in *Tb*PTR1 and *Lm*PTR1, respectively. Hydrogen bonds are represented by brown dashed lines. Further IF docking poses are shown in Figures S7 and S8.

result in selectivity benefits from this approach: The tail region is enclosed by more hydrophobic moieties in parasite DHFR than in the hDHFR off-target (Figure 4A), and residues surrounding the tail have previously been demonstrated to show differing conformational variability in the crystal structures when comparing parasitic targets with the off-target.[31]

To combine exploitation of the differing patterns of hydrophobic residues in the tail environments of targets and off-targets with improved enclosure in PTR1 (Figure 4A,B), we further modified the tail to an unsubstituted piperidine (**4c**) or replaced piperidine with an unsubstituted benzene (**4d**). Compound **4e**, with benzene attached via a flexible ethyl linkage to an MTX-like amide, can benefit from nonpolar and aromatic residues surrounding the tail in PTR1 and parasite DHFR and, according to docking predictions, readily adapt to their differing placements in the on-targets; see Figure 5E,F. The docking studies additionally suggest that the flexible aromatic tail can form cation−π interactions with positively charged residues in the entrance of the DHFR pocket (e.g., Arg59 of *Tb*DHFR, Figures 4A and 5F). Additional hydrophobic residues in the target pocket entrance regions, like Pro99 of *Tb*PTR1 (Figure 4A), can be targeted with an altered geometry in combination with methoxylations: **4f** and **4g** combine a one-carbon spacer between N10 and PABA and amide-linked methoxylated tail portions. In addition, an etheryl linkage to a nonsubstituted (**4h**), methoxylated (**4i**), or trimethoxylated (**4j**) benzyl group was explored. Compounds **4f−4j** were collectively designed to interact with the different hydrophobic, aromatic, and positively charged surrounding residues found around the tail region in the various targets (Figure 4A).

Taken together, the tail series comprises 10 new pteridines (**4a−4j**, Figure 6) with modified tails to target residue patterns

https://doi.org/10.1021/acs.jmedchem.2c00232
J. Med. Chem. 2022, 65, 9011−9033

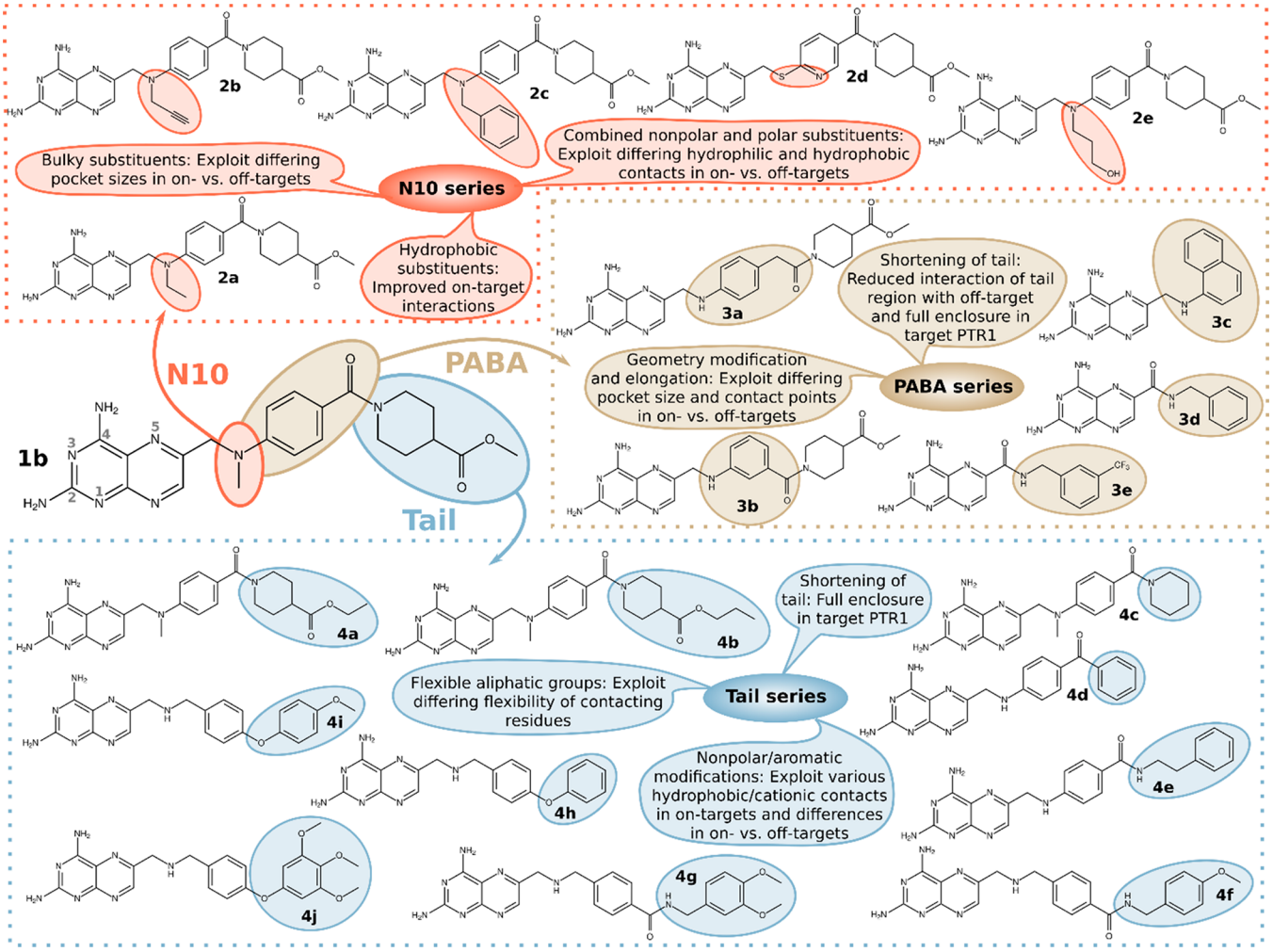

Figure 6. Overview of the modifications in the N10, PABA, and Tail modules explored in the designed compound series with respect to the reference compound **1b**. Synthesized members of each designed series are shown in the framed boxes along with the key objectives addressed with the respective modifications. See text for details.

Scheme 1. Synthesis of Derivatives of Compound 29[a]

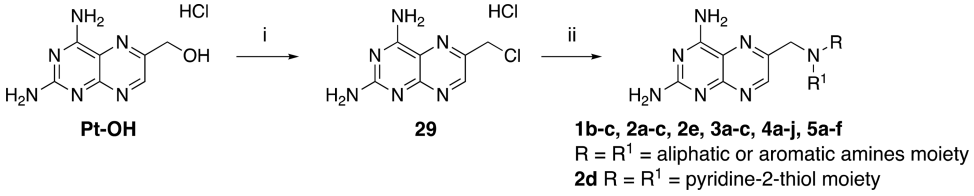

[a]Reagents and conditions: (i) $SOCl_2$, reflux, 12 h, 70% yield; (ii) **29** (1.2 equiv), corresponding amine derivative (1 equiv), K_2CO_3 (3 equiv), KI (0.1 equiv), DMA, 60°C, 20′−30′ MW.

distinguishing on- and off-targets and the distinct surroundings of the tail in PTR1 vs DHFR.

Synthesis of Pteridine Derivatives with High Yield. A total of 26 new 2,4-diaminopteridine derivatives and the reference compounds **1b** and **1c** were (re)synthesized as reported in Schemes 1−8. We applied our methodology for an improved reaction yield of the chemical pteroid step to provide a key intermediate for most of the designed compounds.[33] Displacement of the chloride of 6-(chloromethyl)pteridine-2,4-diamine hydrochloride (**29**, Scheme 1) by the appropriate substituted anilines and aliphatic amino derivatives was carried out in *N*,*N*-dimethylacetamide (DMA) at 60 °C microwave (MW) to provide **1b**,**c**, **2a**−**e**, **3a**−**c**, **4a**−**j**, and **5a**−**f** in high yields of 70−90% with reduced reaction time (Schemes 2−7).[33]

The PABA amine functionalization was achieved by selective alkylation of primary amines to secondary amines using nitriles as alkylating reagents with Pd/C for intermediates **32** and **33**.[34,35] Conventional alkylation of the latter with propargyl bromide or (bromomethyl)benzene resulted in derivatives **34** and **35**, respectively (Scheme 2).

The reductive alkylation of amines using nitriles was also used to obtain **51** and **74** in Schemes 3 and 7. The isonipecotic acid derivatization was achieved via Fischer esterification using the reagent solvents propanol (**37**) and EtOH (**38**), respectively;

https://doi.org/10.1021/acs.jmedchem.2c00232
J. Med. Chem. 2022, 65, 9011−9033

Scheme 2. Synthesis of Compounds 1b,c, 2a−c, 2e, 4a−c, and 5c, and Intermediates 32−35, 37, 38, and 40−49[a]

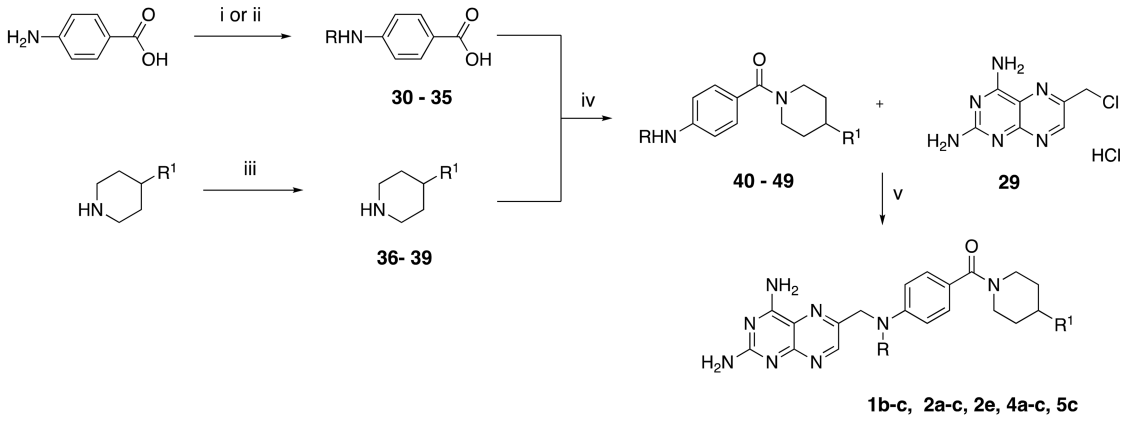

	R=	R¹=
30	CH_3	_
31	H	_
32	CH_2CH_3	_
33	$CH_2CH_2CH_2OH$	_
34	CH_2CCH	_
35	$CH_2C_6H_5$	_
36	_	$COOCH_3$
37	_	$COOCH_2CH_2CH_3$
38	_	$COOCH_2CH_3$
39	_	H

		R=	R¹=
40	1b	CH_3	$COOCH_3$
41	1c	H	$COOCH_3$
42	2a	CH_2CH_3	$COOCH_3$
43	2e	$CH_2CH_2CH_2OH$	$COOCH_3$
44	2b	CH_2CCH	$COOCH_3$
45	4b	CH_3	$COOCH_2CH_2CH_3$
46	4a	CH_3	$COOCH_2CH_3$
47	5c	CH_2CH_3	$COOCH_2CH_3$
48	2c	$CH_2C_6H_5$	$COOCH_3$
49	4c	CH_3	H

[a]Reagents and conditions: compounds **30**, **31**, **36**, and **39** were purchased from Sigma; (i) acetonitrile or 3-hydroxypropanenitrile, 10% Pd/C, NH_4OAc (1 equiv), CH_3OH, H_2, rt, 24−36 h (**32**, **33**); (ii) alkyl halide (propargyl bromide, (bromomethyl)benzene) (0.5 equiv), K_2CO_3 (2 equiv), DMF dry, rt, 24 h (**34**, **35**); (iii) $SOCl_2$ (4 equiv), propanol (for **37**), EtOH (for **38**), reflux, 7−12 h (89 and 96% yield); (iv) EDC·HCl (1.1 equiv), HOBt (0.1 equiv), TEA (2−3 equiv), DMF, rt, overnight (**40**−**49**); (v) **29** (1.2 equiv), corresponding amine derivative (1 equiv), K_2CO_3 (3 equiv), KI (0.1 equiv), DMA, 20′ MW (**1b,c**, **2a−c**, **2e**, **4a−c**, **5c**).

Scheme 3. Synthesis of Compounds 3a and 5a,b[a]

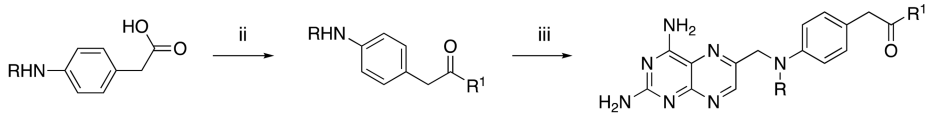

50 R = H
51 R = $CH_2CH_2CH_2OH$

52 R = H, R^1 = 36
53 R = $CH_2CH_2CH_2OH$, R^1 = 53a
54 R = $CH_2CH_2CH_2OH$, R^1 = 54a

3a R = H, R^1 = **52a**
5a R = $CH_2CH_2CH_2OH$, R^1 = **53a**
5b R = $CH_2CH_2CH_2OH$, R^1 = **54a**

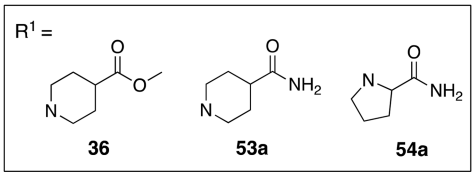

[a]Reagents and conditions: (i) 3-hydroxypropanenitrile, 10% Pd/C, NH_4OAc (1 equiv), CH_3OH, H_2, rt, 24 h (**51**); (ii) EDC·HCl (1.1 equiv), HOBt (0.1 equiv), TEA (2−3 equiv), DMF, rt, overnight (**52**−**54**); (iii) **29** (1.2 equiv), corresponding amine derivative (1 equiv), K_2CO_3 (3 equiv), KI (0.1 equiv), DMA, 20′ MW (**3a**, **5a,b**).

methyl isonipecotate (**36**) and piperidine (**39**) were purchased from Sigma (Scheme 2).

The intermediate acid derivatives **30**−**35** and **d** and **e** were condensed to amides through a coupling reaction with the respective amines **36**−**39** and **g** using EDC·HCl in dimethylformamide (DMF) as the coupling agent to provide the intermediate products **40**−**49**, **71**, **72**, and **75**, which were then made to react with **29** to obtain the final compounds (**1b,c**, **2a−d**, **3b**, **4a−c**, **4e**, **5c**; Schemes 2, 6, 7).

Using the same method, we synthesized the elongated compounds **3a**, **4f−g**, and **5a,b**, characterized by a carbon spacer in the PABA moiety (Schemes 3 and 4).

To obtain **4f,g** (Scheme 4), an additional protection step reaction to guide selective amide functionalization was

https://doi.org/10.1021/acs.jmedchem.2c00232
J. Med. Chem. 2022, 65, 9011−9033

Scheme 4. Synthesis of Compounds 4f,g[a]

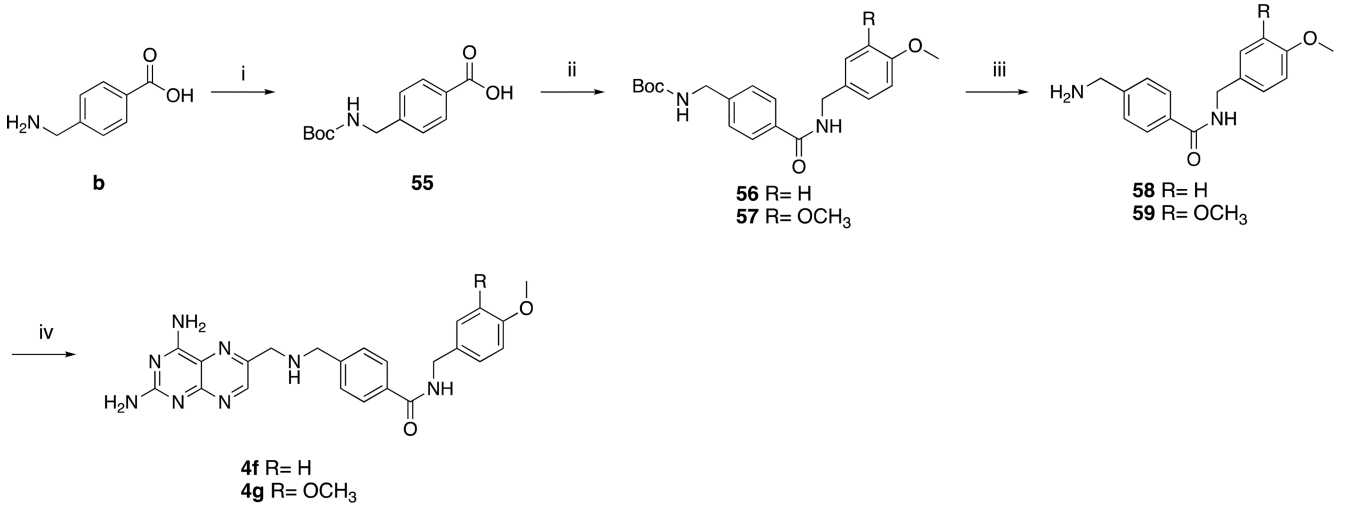

[a]Reagents and conditions: (i) di-*tert*-butyl pyrocarbonate (1.05 equiv), dioxane/H_2O/1 N NaOH 1/1/1 V/V/V, rt, 6 h (**55**); (ii) EDC·HCl (1.1 equiv), HOBt (0.1 equiv), TEA (2−3 equiv), DMF, rt, overnight (**56** and **57**); (iii) TFA, DCM, rt (**58** and **59**); (iv) **29** (1.2 equiv), corresponding amine derivative (1 equiv), K_2CO_3 (3 equiv), KI (0.1 equiv), DMA, 20′ MW (**4f,g**).

Scheme 5. Synthesis of Compounds 4h−j and 5e,f[a]

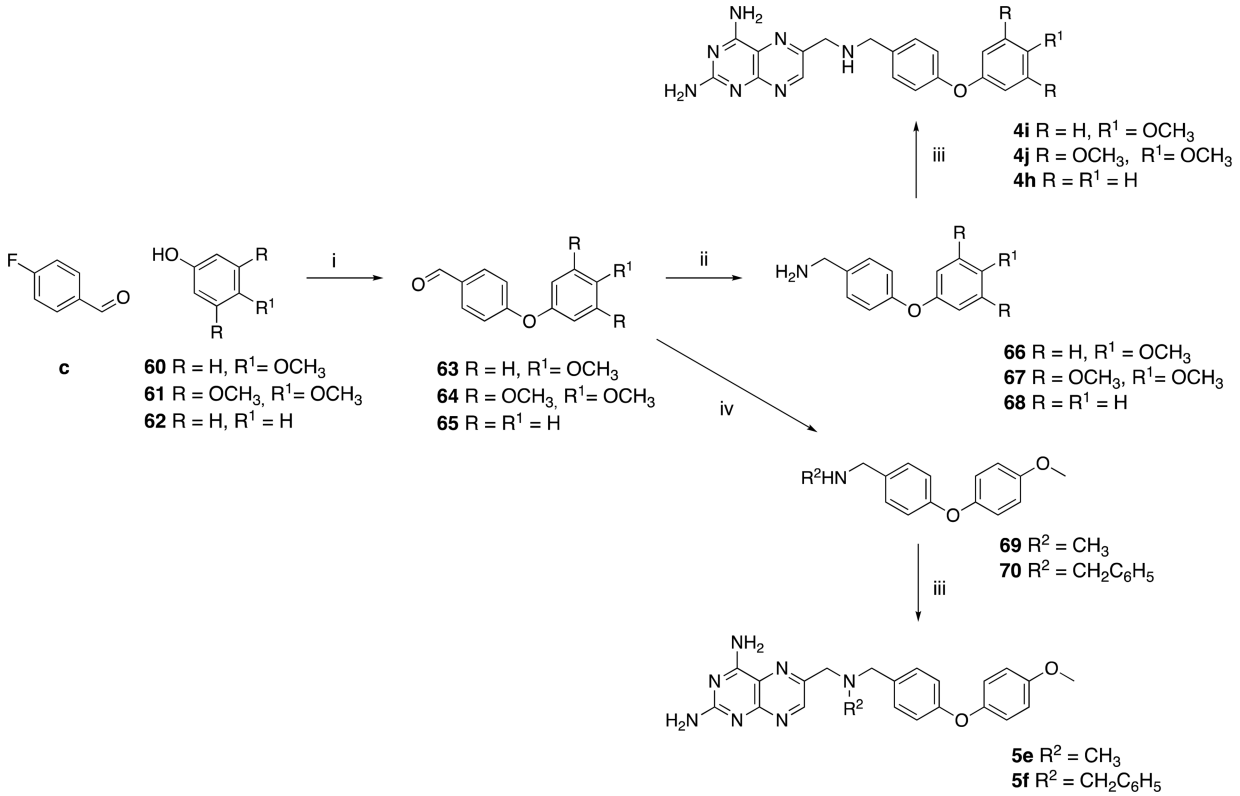

[a]Reagents and conditions: (i) K_2CO_3 (3 equiv), DMF, reflux, 16−18 h (**63−65**); (ii) NH_2OH·HCl (1.2 equiv), EtOH, rt, >1 h followed by Zn dust (2.5 equiv) in 12 M HCl (4 equiv), rt, 15′ (**66−68**); (iii) **29** (1.2 equiv), corresponding amine derivative (1 equiv), K_2CO_3 (3 equiv), KI (0.1 equiv), DMA, 20′ MW (**4h−j**, **5e,f**); (iv) methylamine (for **69**) or benzylamine (for **70**), EtOH dry, 60°C, 3 h, then $NaBH_4$ (1.5 equiv), rt, 2 h.

necessary. The selectivity was achieved via Boc protection in the first step of the reaction of **b** to obtain **55**, which was then coupled with the respective aliphatic amine to give **56** and **57**. The target amines were finally obtained by a deprotection step carried out in 30−40% trifluoroacetic acid/dichloromethane (TFA/DCM) in quantitative yield.

The phenoxyphenyl−methanamine derivative intermediates (Scheme 5) were synthesized starting from 4-fluorobenzaldehyde and the respective phenol derivates **60−62** by an S_NAr reaction. Subsequently, the primary amines **66−68**,[36] or functionalized amines **69** and **70** (obtained via a one-pot reductive step), were reacted with **29** to obtain **4h−j** and **5e,f**.

https://doi.org/10.1021/acs.jmedchem.2c00232
J. Med. Chem. 2022, 65, 9011−9033

Scheme 6. Synthesis of Compounds 3b and 2d[a]

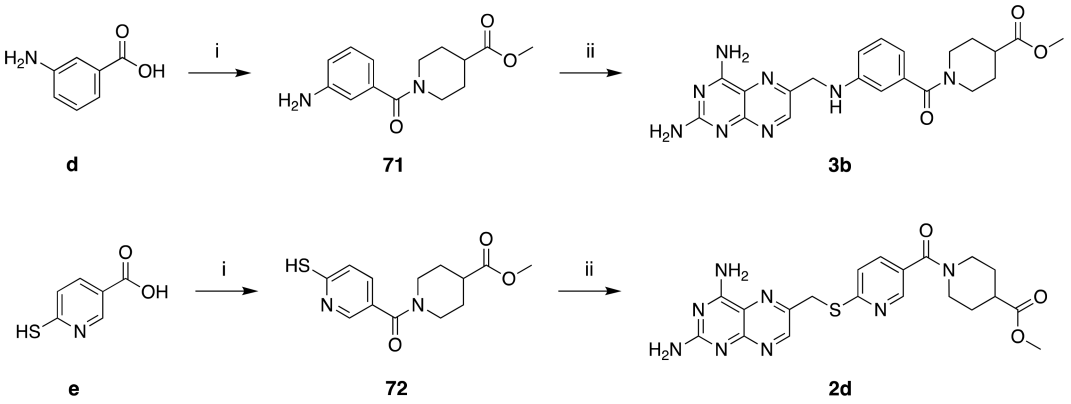

[a]Reagents and conditions: (i) EDC·HCl (1.1 equiv), HOBt (0.1 equiv), TEA (2−3 equiv), DMF, rt, overnight (**71** and **72**); (ii) **29** (1.2 equiv), corresponding amine derivative (1 equiv), K_2CO_3 (3 equiv), KI (0.1 equiv), DMA, 20′ MW (**3b**, **2d**).

Scheme 7. Synthesis of Compounds 3c, 4d,e, and 5d[a]

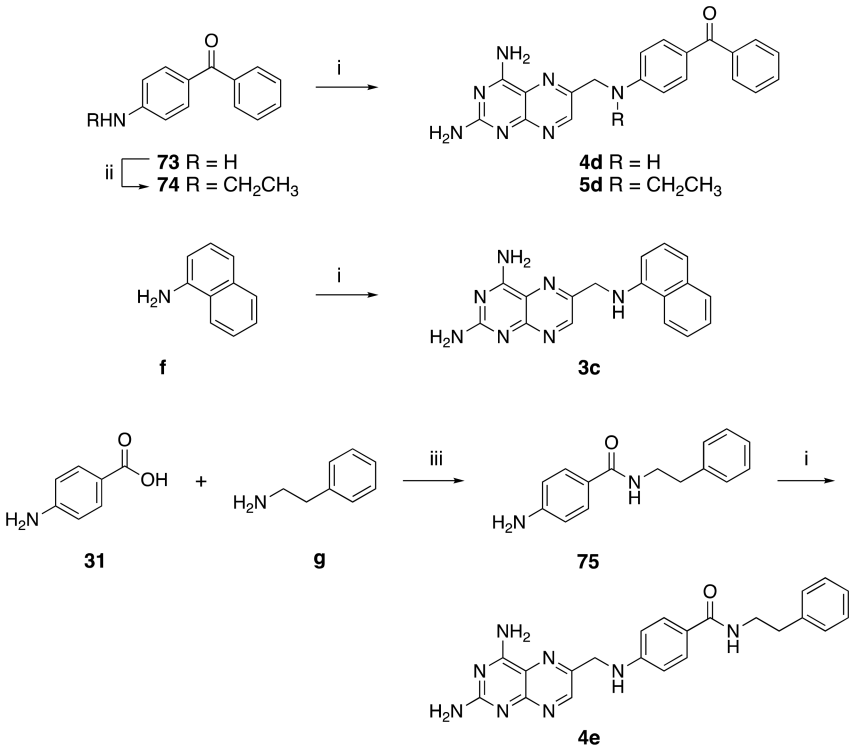

[a]Reagents and conditions: (i) **29** (1.2 equiv), corresponding amine derivative (1 equiv), K_2CO_3 (3 equiv), KI (0.1 equiv), DMA, 30′ MW (**3c**, **4d**,**e**, and **5d**); (ii) acetonitrile, 10% Pd/C, NH_4OAc (1 equiv), CH_3OH, H_2, rt, 24−36 h (**74**); (iii) EDC·HCl (1.1 equiv), HOBt (0.1 equiv), TEA (2−3 equiv), DMF, rt, overnight (**75**).

Scheme 8. Synthesis of Compounds 3d,e[a]

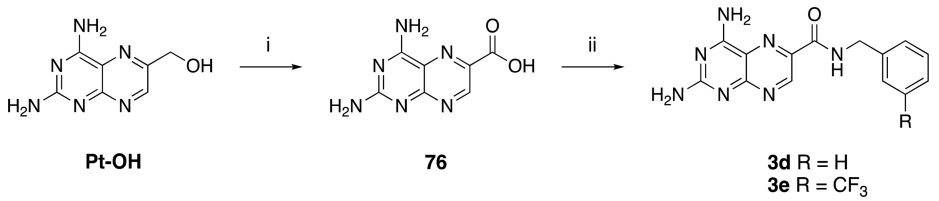

[a]Reagents and conditions: (i) $KMnO_4$, acetone/0.5 M phosphate buffer at pH 7 (1:1 V/V); (ii) EDC·HCl (1.1 equiv), HOBt (0.1 equiv), TEA (2−3 equiv), DMF, rt, overnight.

https://doi.org/10.1021/acs.jmedchem.2c00232
J. Med. Chem. 2022, 65, 9011−9033

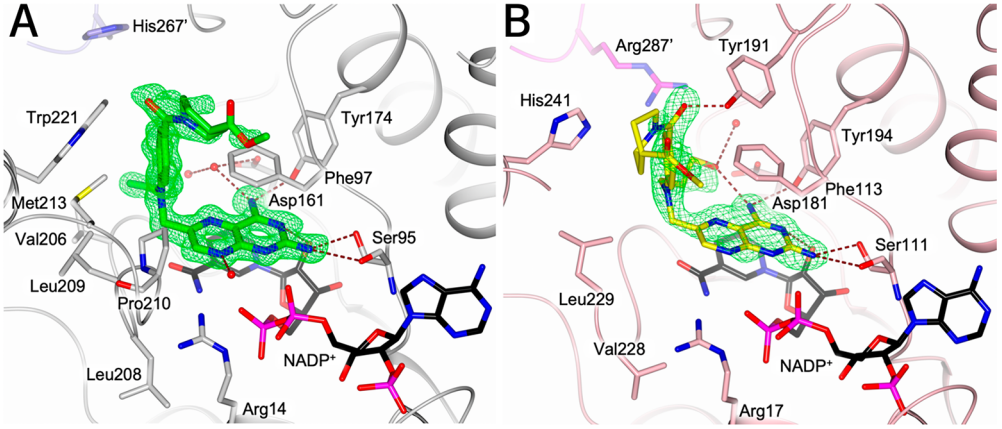

Figure 7. Views of the binding sites of crystal structures of complexes of pteridine-based inhibitors in *Tb*PTR1 and *Lm*PTR1 determined in this work, which confirm the predicted MTX-like binding modes. (A) **2a** (green carbons) in *Tb*PTR1 (gray cartoon, His267′ from the neighboring subunit in lavender) and (B) **2e** (yellow carbons) in *Lm*PTR1 (pink cartoon, Arg287′ from the neighboring subunit in magenta). Water molecules are shown as red spheres, and the inhibitors are surrounded by the omit map (green wire) contoured at the 2.5 σ level. Interacting residues and the NADPH/NADP$^+$ cofactor are shown in sticks (carbons colored according to protein and black, respectively). Hydrogen bonds are represented by brown dashed lines.

Compounds **3c**, **4d**, and **5d**, with a higher steric hindrance, were obtained with a slightly increased reaction time in a good yield. Finally, to obtain **3d**,**e**, it was necessary to first perform an oxidation reaction. Treatment of Pt−OH in acetone/0.5 M phosphate buffer at pH 7 (1:1 v/v) with $KMnO_4$ gave the oxidized analogue **76**, which was subsequently coupled with the selected aliphatic amine to obtain the desired amides (Scheme 8).

Crystal Structures for the PTR1 Targets Confirm the Predicted Interactions and That the Pteridine Derivatives Adopt a Methotrexate-Inhibitor-Like Orientation. The structures of *Tb*PTR1 with two new pteridines, **2a** and **2e**, and that of *Lm*PTR1 with **2e**, were determined to 1.20, 1.11, and 2.10 Å resolution, respectively (see Tables S2 and S3). The structures contain functional enzyme tetramers in the crystallographic asymmetric unit with a similar structure to those previously determined.[37,38] In all complexes, the compounds adopt MTX-like binding modes (Figure 7A,B).

In line with the docking predictions, the overall structure of the *Tb*PTR1 complexes resembles the complex with **1b** (compare Figure 7A with 3C). In agreement with the design objective, the *N*-ethyl moiety of **2a** was found to form van der Waals interactions with Val206 and Trp221 on the hydrophobic side of the pocket (Figure 7A). The bulkier N-propylhydroxyl moiety of **2e** forms direct and water-mediated hydrogen bonds with Asp161 and receives an intramolecular hydrogen bond from the amine in position 4 on the pteridine system (Figure S2C). The structure of *Lm*PTR1 in complex with **2e** (Figure 7B) closely resembles that observed in *Tb*PTR1, except for the terminal piperidine moiety (Figure S2C,D). The latter moiety is highly flexible—a possible orientation is reported in the crystal structure, but further orientations cannot be excluded.

Designed Pteridine Derivatives Have Improved Target and Off-Target Enzyme Inhibitory Activities. The measured inhibitory activities of compounds **2a**−**e**, **3a**−**e**, and **4a**−**j** against the targets *Tb*PTR1, *Tb*DHFR, *Lm*PTR1, and *Lm*DHFR and the off-targets hDHFR and hTS are given in Figure 8 and Table S1. All inhibitory activities are reported as IC_{50} values, which are commonly used to characterize and rank compounds when screening for enzyme inhibition in drug discovery projects.[39] Overall, the inhibitory activities against the PTR1 targets for the designed compounds are improved, as are PTR1 vs off-target selectivities. Indeed, for a small number of compounds (**2c**, **2d**, **4c**, **4d**, **4e**, **5c**, and **5d**), the IC_{50} values for inhibition were determined to be either 1 nM or less than 0.1 nM against *Tb*PTR1. As the *Tb*PTR1 assay makes use of low nanomolar concentrations of enzyme, for these very potent compounds, the tight binding limit was approached, and therefore, accurate values of the IC_{50} values could not be determined.[40] Representative dose−response curves are shown in the Supporting Information, showing that only part of the response range could be measured for these compounds for which the IC_{50} value could also be rather sensitive to any possible errors in dilution or determination of inhibitor or enzyme active site concentration.

N10 Modifications Yield Improved PTR1 Inhibitors with Similar Selectivity Trends for Parasite DHFRs. The N10-modified compounds (**2a**−**e**; Figure 6) are improved PTR1 inhibitors in comparison to **1b**, except for **2a** (**1b** IC_{50} *Tb*PTR1 50 nM, *Lm*PTR1 1 μM; N10 series IC_{50} *Tb*PTR1 < 0.1−90 nM; *Lm*PTR1 0.02−13.3 μM; Figure 8). **2c** is the best in the series with IC_{50} < 0.1 nM against *Tb*PTR1 and an IC_{50} of 20 nM against *Lm*PTR1.

All compounds are roughly similar to **1b** in parasite DHFR inhibition (**1b** IC_{50} *Tb*DHFR and *Lm*DHFR 0.3 μM; N10 series IC_{50} *Tb*DHFR 0.4−2.4 μM, *Lm*DHFR 0.5−9.4 μM), and selectivities over hDHFR range from 7- to 66-fold for *Tb*DHFR and 9- to 110-fold for *Lm*DHFR, which are somewhat lower than for **1b** (SI *Tb*DHFR/hDHFR = 164 and *Lm*DHFR/hDHFR = 167). Thus, mainly PTR1 inhibition benefits from the selected N10 modifications.

PABA Modifications Lead to Strong Variations in the Target Inhibition Profile. The modifications of the PABA moiety in the PABA series (compounds **3a**−**e**; Figure 6) distinctly affect the inhibitory activities against the targets. Smaller compounds with well-enclosed binding poses show varying improvements in inhibitory activity for different PTR1 variants: **3c**, in contrast to most of the studied pteridines, is equipotent toward *Lm*PTR1 and *Tb*PTR1 (IC_{50} 10 nM). This notable improvement of *Lm*PTR1 activity is in line with its predicted good steric fit to the *Lm*PTR1 binding pocket shape (compare Figures 4C and 5C). Full enclosure and stabilizing interactions with hydrophobic residues lining the pocket entrance likewise probably contribute to an around 10-fold

https://doi.org/10.1021/acs.jmedchem.2c00232
J. Med. Chem. 2022, 65, 9011−9033

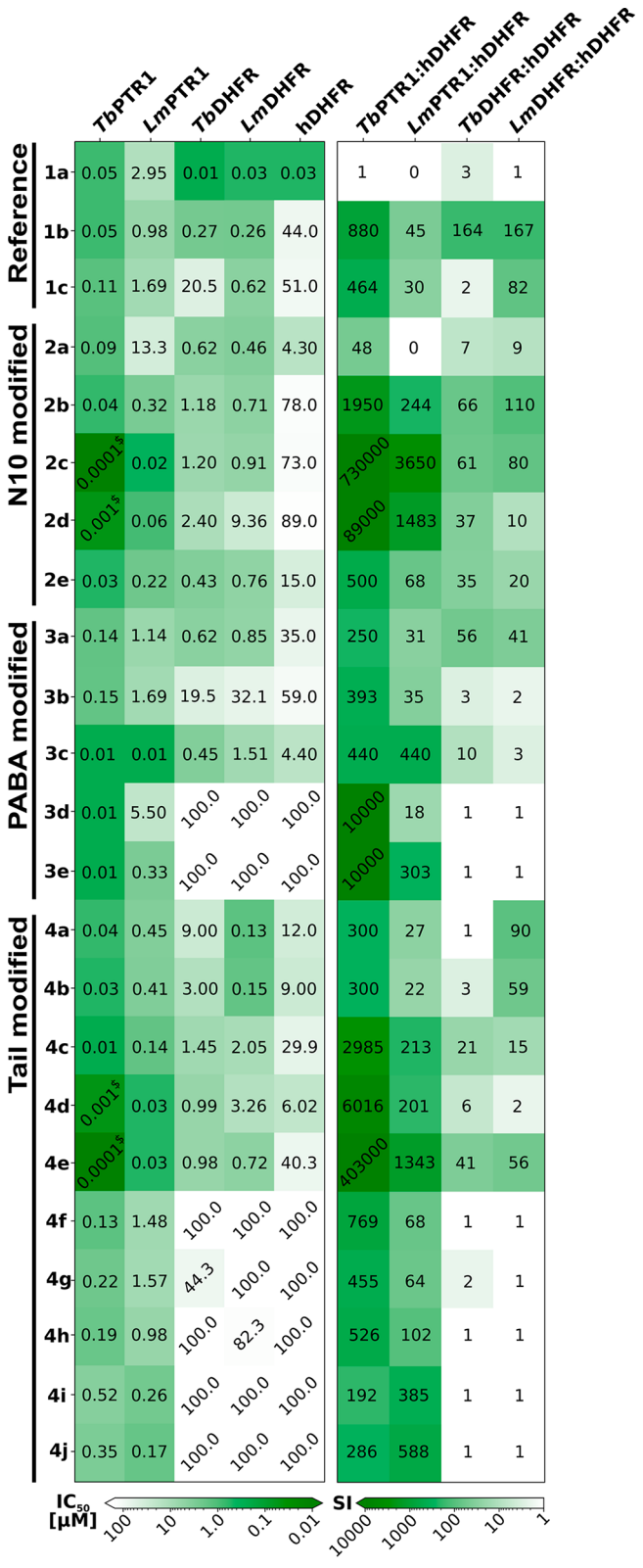

Figure 8. Inhibitory activities (IC_{50} values, left) and selectivities (selectivity indices (SI), right) of compounds of the designed N10-, PABA-, and Tail-modified series and selected reference compounds against the targets *Tb*PTR1, *Lm*PTR1, *Tb*DHFR, and *Lm*DHFR and the off-target hDHFR. All values, as well as data for hTS, are reported in Table S1. Greener boxes show higher inhibition and selectivity. $ indicates that a precise activity value could not be determined as the tight binding limit was approached.

higher potency of **3d** and **3e** against *Tb*PTR1 than the most similar reference compound **1c** (lacking an N10 substitution) (IC_{50} **3d**, **3e**: 10 nM; **1c**: 110 nM).

Whereas **3d** and **3e** do not show inhibitory activity against the parasite DHFR targets, **3c** shows similar activity against *Lm*DHFR to **1c** (IC_{50} 1.5 and 0.6 μM, respectively) and displays higher activities against both *Tb*DHFR (IC_{50} **1c**: 20.5 μM; **3c**: 0.5 μM) and hDHFR (IC_{50} **1c**: 51 μM; **3c**: 4 μM). A one-carbon spacer to shift the position of the PABA carbonyl in **3a** with respect to **1c** improves inhibition of *Tb*DHFR (IC_{50} 0.6 μM) while not significantly affecting inhibition of *Lm*DHFR and hDHFR. Thus, **3a** is more selective against TbDHFR than the reference **1c** (SI: 56 vs 2).

Taken together, alterations to the PABA moiety, due to its central location in the compound scaffold, different pocket sizes, and surrounding residue patterns in targets (Figure 4A) display highly variable effects on the activity profiles.

Alterations in Tail Geometry Boost PTR1 Inhibition but Can Reduce DHFR Inhibition. In the Tail-modified series (compounds **4a**−**j**; Figure 6), hydrophobic and aromatic residues lining the pocket entrance region of PTR1 were exploited by either tail elongation or shortening. The interactions of these residues with the flexible aromatic tail of **4e** (see Figure 5E) likely contribute to the boost of the IC_{50} against *Tb*PTR1 to the subnanomolar range and to 30 nM against *Lm*PTR1; these are 1000-fold and 57-fold improvements, respectively, in PTR1-inhibitory potencies compared to reference compound **1c**. The shortened tails of **4c** (unsubstituted piperidine) and **4d** (benzene) are stabilized by the same residues and likely benefit from a better enclosure in the PTR1 pocket. Both compounds show improved *Tb*PTR1 and *Lm*PTR1 inhibition compared to **1b** (IC_{50} *Tb*PTR1 **4c**: 10 nM, **4d**: 1 nM vs **1b**: 50 nM; *Lm*PTR1 **4c**: 0.1 μM, **4d**: 0.03 μM vs **1b**: 1.0 μM).

However, shortening of the tail diminishes the inhibition of parasite DHFR, whereas it either does not affect or increases inhibition of the off-target hDHFR. Revisiting the docking predictions provides a possible explanation for this: The piperidine/benzene groups in the tails of **4c** and **4d** can form more extended hydrophobic interactions with Phe31 of hDHFR than with the corresponding methionine in the parasite DHFR variants (Figure 9). In the parasite protein, moreover, Asn64 in the pocket entrance of hDHFR is replaced by phenylalanine, which, upon interaction with the compound tail, becomes solvent-exposed.

Pocket size and interaction pattern differences between *Lm*DHFR and other DHFR variants, as also discussed for the PABA series, also affect the Tail-modified compounds: for instance, **4d** is more active against both *Tb*DHFR and hDHFR than **1c** (IC_{50} *Tb*DHFR 1 vs 21 μM, hDHFR 6 vs 51 μM), while both compounds show similar activity for *Lm*DHFR.

Summary of the Compound Activity Profiles for the N10, PABA, and Tail-Modified Series. Taken together, most of the new pteridine derivatives display 1−2-fold greater inhibition of *Tb*PTR1 than *Lm*PTR1 and are more or equally active against PTR1 than the reference compound **1b**. The nanomolar to subnanomolar PTR1 inhibitors show improved selectivity for PTR1 over the off-target hDHFR by up to about 3 orders of magnitude (**2c**, **4e**: *Tb*PTR1 IC_{50} < 0.1 nM; SI > 400 000) (Figure 8). The IC_{50} against hDHFR is typically greater than 100 μM, whereas inhibitory activities against *Tb*DHFR and *Lm*DHFR are higher. For parasite DHFR, the compounds with the best inhibitory activities have similar IC_{50}

https://doi.org/10.1021/acs.jmedchem.2c00232
J. Med. Chem. 2022, 65, 9011−9033

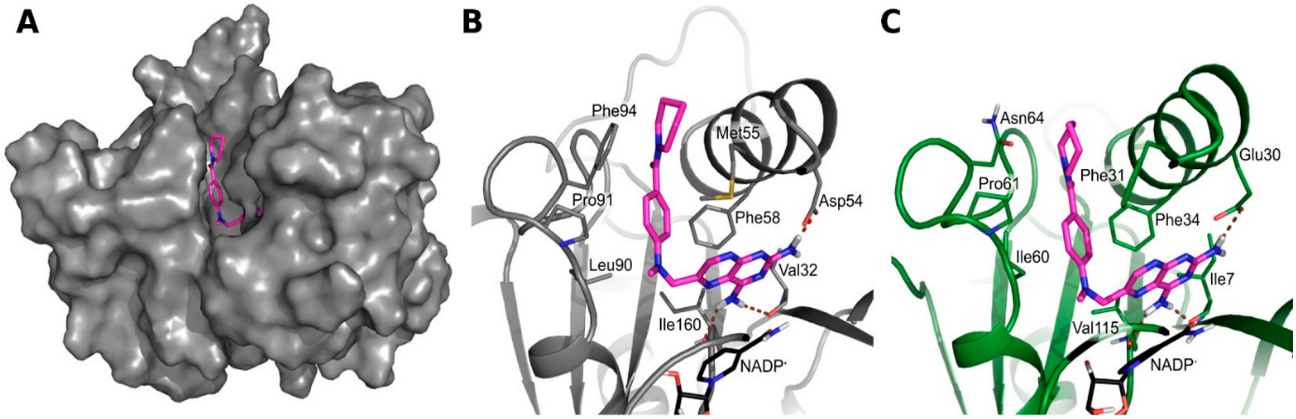

Figure 9. Docking poses for compound **4c** from the Tail series (magenta carbons) in (A,B) *Tb*DHFR and (C) hDHFR, showing differences in exposure and interactions of the PABA and Tail moieties in the two DHFRs. (A) *Tb*DHFR pocket accommodates **4c** with its tail enclosed by surrounding residues. hDHFR has a similar shape. *Tb*DHFR is shown in a gray surface representation. (B,C) Views of the binding sites of *Tb*DHFR and hDHFR, which are shown in cartoon representation in gray and green, respectively. Important interacting residues and the NADPH/$NADP^+$ cofactor (black carbons) are shown as sticks. Hydrogen bonds are indicated by brown dotted lines. While the orientations of **4c** are rather similar in both DHFR variants, the tail moiety is more solvent-exposed in *Tb*DHFR: the PABA benzene and piperidine of **4c** compete for interactions with Phe94 of *Tb*DHFR, which thereby becomes exposed to the solvent. In hDHFR, the corresponding exposed residue is the polar Asn64, and the tail of **4c** can interact with Phe31 deeper in the pocket, rendering the mode of binding more favorable in hDHFR. The results are presented for N1-deprotonated compounds, but similar observations were made with N1-protonated compounds (Figure S6).

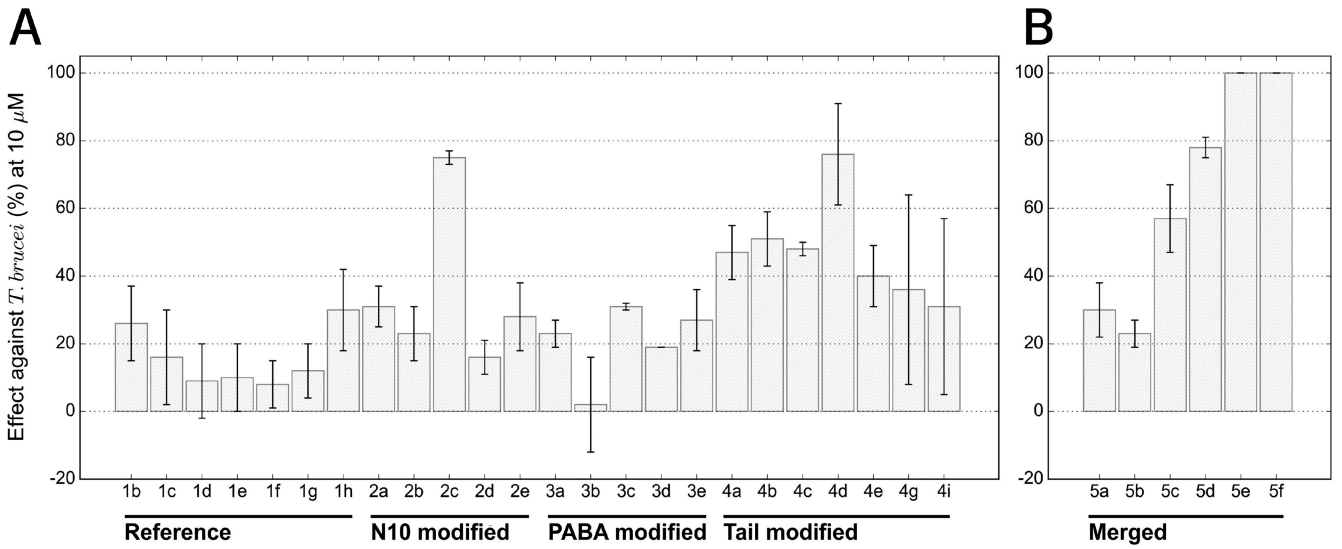

Figure 10. Antiparasitic activity expressed as percentage of inhibition against *T. brucei brucei* for reference compounds and members of the N10-, PABA-, and Tail-modified series (A) and the selected representatives of the merged *in silico* library (B). The average of at least three independent determinations is shown with the standard deviation. The inactive compounds in the Tail-modified series, **4f**, **4h**, and **4j** were omitted. Activities can be found in Table S7.

values to **1b** (e.g., *Lm*DHFR IC_{50} **4a**: 0.13 μM, **4b**: 0.15 μM, and **1b**: 0.26 μM). Thus, the newly designed compounds show improved target inhibitory profiles, particularly for the PTR1 targets, and overall good selectivity for the parasitic proteins.

Inhibitory Activity against *T. brucei* Is Related to the Hydrophobicity of the Compounds. Following the assessment of the improvement on the target inhibition level, we next determined the antiparasitic effect on *T. brucei brucei* Lister 427 bloodstream forms and *L. infantum* intramacrophage amastigotes (Figure 10A and Table S7). The *Lm*PTR1 and *Lm*DHFR proteins are highly similar to the corresponding *L. infantum* proteins (91 and 96% sequence identity, respectively), but in spite of the improved effect on both target proteins, the designed pteridines are mostly inactive against *L. infantum*. In contrast, the compounds show activity against *T. brucei.*

The multiple correlation coefficient between the *Tb*PTR1 and *Tb*DHFR IC_{50} values and the *T. brucei* bloodstream form inhibition is R = 0.35 (eq 3, SI), indicating that the levels of target enzyme inhibition are, for the current compounds, only weakly correlated with the exhibited antiparasitic effect when assuming a linear correlation. PTR1 inhibition alone shows a Pearson correlation R = 0.34 with *T. brucei* inhibition, whereas R is only 0.24 for DHFR inhibition, possibly because all studied compounds are much stronger inhibitors of PTR1 than DHFR. The low correlation for DHFR inhibition might also arise because of the competition from the high folate concentration in the medium in the parasite assays.

Another reason for the low correlations between parasite and target protein inhibition could be transport issues. For example, the charged compound tail and possible polyglutamylation of

https://doi.org/10.1021/acs.jmedchem.2c00232
J. Med. Chem. 2022, 65, 9011−9033

Table 1. Descriptors with Significant Correlations with the Observed Inhibitory Effect on *T. brucei* for the Reference Compounds and Pteridines of the N10-, PABA-, and Tail-Modified Series Calculated with QikProp[43a]

predicted property	QPlogKp	QPlogPo/w	QPlogKhsa	cohesive index	CIQPlogS
R	0.55	0.49	0.47	−0.41	−0.54
R^2	0.30	0.24	0.22	0.17	0.29
P-value	0.003	0.01	0.01	0.04	0.004
resampling recovery rate (%)	100	96	96	56	96
optimization direction	↑	↑	↑	↓	↓
covered range	−6.62 − −3.60	−1.02−2.92	−0.85−0.35	0.02−0.04	−6.71 − −3.19
recommended range	−8.00 − −1.00	−2.00−6.50	−1.50−1.50	0.00−0.05	−6.50−0.50

[a]QPlogKp: Predicted skin permeability, log K_p; QPlogPo/w: Predicted octanol/water partition coefficient. QPlogKhsa: Prediction of binding to human serum albumin. Cohesive index: Index of cohesive interaction in solids, (number of hydrogen bond acceptors × number of hydrogen bond donors × 0.5/surface area);[44] CIQPlogS: Conformation-independent predicted aqueous solubility, log S with S in mol dm^{-3} being the concentration of the solute in a saturated solution that is in equilibrium with the crystalline solid. R (Pearson correlation) and R^2 were calculated using the percentage of inhibition of the *T. brucei brucei* Lister 427 bloodstream form at a 10 μM compound concentration as defined in the SI. Only descriptors with at least a Pearson correlation/anticorrelation of 0.40/−0.40 and two-tailed P-values lower than the chosen significance level α of 0.05 are reported. The covered range lists property values obtained for the studied compounds, while the recommended range lists values the properties take for typical drug-like molecules. The resampling recovery rate indicates in how many cases (expressed as percentage) the same property was identified when leaving a single compound out of the data set. The optimization direction indicates whether higher or lower values would putatively lead to improved anti-parasitic effects.

the parent MTX (**1a**) have previously been suggested to influence compound transport.[41,42] All the newly designed pteridines lack the glutamate tail, which may affect their *in vivo* activities, but there might be other structural or physicochemical features that render them more or less active against parasites despite similar target inhibition. For example, for *T. brucei*, we noticed that while **2c** and **4e** have similar effects on the targets *Tb*PTR1 (0.1 nM) and *Tb*DHFR (approximately 1 μM), they differ notably in their inhibitory effect on the parasite bloodstream forms (75 vs 40%).

Therefore, we investigated the correlations of physicochemical properties and ADMET predictors with the measured effect on *T. brucei*; see Table 1. Our aim was to identify which properties were indicative of a better antiparasitic effect, possibly related to better uptake. Overall, only weak correlations of the individual properties with *T. brucei* inhibition were observed (Pearson R: 0.47−0.55 and −0.41 − −0.54; computed as defined in the SI). The strongest correlation was found for the predicted skin permeability, QPlogKp, as a descriptor linked to lipophilicity, (R: 0.55). The logPo/w and the binding to human serum albumin had slightly weaker correlations with the antiparasitic effect (R: 0.49 and 0.47, respectively). For these properties, an increase in the value corresponds with higher anti-*T. brucei* activity. In contrast, some properties showed anticorrelation, for instance, the aqueous solubility and the cohesive index[44] (R: −0.54 and −0.41, respectively). Taken together, the data indicate an improved antiparasitic effect with increased lipophilicity of the studied compounds.

Combined Modifications Yield Pteridines with Both Improved Target Inhibition and Improved Antiparasitic Activity. To explore further derivatives of the studied pteridines, we next designed a merged compound library as follows. The pteridine core scaffold was retained, and the studied compounds were decomposed into fragments of their N10, PABA, and Tail regions and recombined *in silico* in all possible combinations to yield 2014 derivatives (see SI for details). These derivatives were evaluated in docking studies against targets and off-targets and additionally prioritized by the physicochemical marker properties that showed correlations with the anti-*T. brucei* effect (Figure S9). Of the remaining 600 candidates, 6 were selected by expert opinion as representative compounds for synthesis and experimental evaluation (**5a**−**5f**, Figure 11).

Two compounds, **5a** and **5b**, were chosen for their favorable interaction patterns and scores predicted by docking simulations. **5a** combines the N10 hydroxypropyl fragment of **2e**, benzyl in place of the PABA phenyl of **3a**, the tail amide of reference compound **1g**, and, for **5b**, in addition, the tail pyrrolidine of ref **1h**, which replaces the tail piperidine. The activities and predicted interactions in all parasite targets are most similar to **2e**, suggesting the key importance of the hydroxy-propyl substituent to N10 for the target inhibition. Notably, while **5a** is poorly selective for *Tb*DHFR (2-fold) and modestly selective for *Lm*DHFR (31-fold), **5b** is inactive against hDHFR, resulting in SI values of 169 and 113 for *Tb*DHFR and *Lm*DHFR, respectively. Moreover, **5b** has SI values over hDHFR of about 25 000 for *Tb*PTR1 and 588 for *Lm*PTR1. However, in contrast to most compounds, **5b** displays a weak inhibition of hTS (IC_{50} 29 μM, Table S1).

Four additional compounds (**5c**−**5f**, Figure 11) were prioritized based on the physicochemical marker properties. Compound **5c** combines fragments of ethyl modification to N10 of **2a** and the tail ethyl ester of **4a**. Due mainly to the tail ester, this modification improves the inhibition for both *Tb*PTR1 (IC_{50} 1 nM) and *Lm*PTR1 (IC_{50} 0.1 μM). The activity against *Tb*DHFR is similar to that of the N10-modified parent **2a**, whereas *Lm*DHFR and hDHFR inhibition are again influenced by the tail modification (IC_{50} *Lm*DHFR **5c**: 0.2 μM, **4a**: 0.1 μM; hDHFR **5c**: 13 μM, **4a**: 12 μM). Compound **5d** merges the ethyl N10 fragment of **2a** with the unsubstituted benzene of **4d**. In *Tb*PTR1, this boosts the nanomolar IC_{50} of **4d** to the subnanomolar range, while the activity toward *Lm*PTR1 remains similar to **4d**. This profile can be related to the N10 ethyl, which seems disfavored in *Lm*PTR1 as judged by the modest inhibition of the parent **2a** (IC_{50} 13.3 μM).

Compounds **5e** and **5f** combine the ethylphenyl(4-methoxyphenyl) ether scaffold of **4i** with the benzyl and methyl N10 modifications from **2c** or **1b**, respectively. Both compounds are nanomolar inhibitors of both PTR1 variants. The parent compounds, **2c** and **1b**, inhibit the parasite DHFR variants at micromolar to submicromolar levels, while **4i** is inactive against all variants of DHFR. The combination with a favorable N10 substitution is able to restore medium micromolar anti-DHFR

https://doi.org/10.1021/acs.jmedchem.2c00232
J. Med. Chem. 2022, 65, 9011−9033

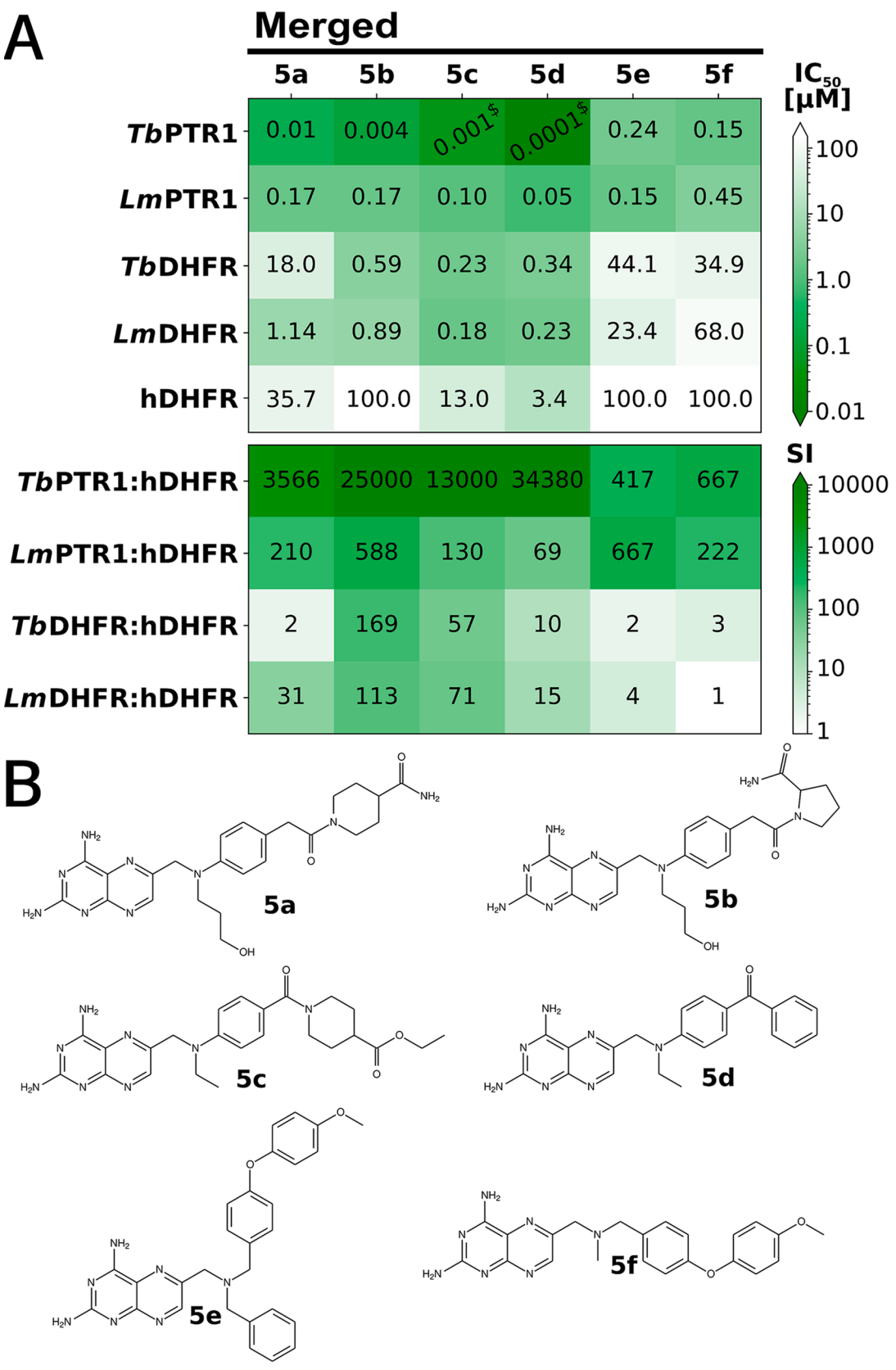

Figure 11. Inhibitory activities, selectivities, and structures of the merged series of six pteridine derivatives. (A) Activity heatmap in the top panel shows IC_{50} values for the targets *Tb*PTR1, *Lm*PTR1, *Tb*DHFR, and *Lm*DHFR and the off-target hDHFR. All values, as well as data for hTS, are reported in Table S1. $ indicates that a precise activity value could not be determined as the tight binding limit was approached. In the bottom panel, selectivity indices are reported. (B) Structures of the selected and synthesized pteridines in the merged series.

https://doi.org/10.1021/acs.jmedchem.2c00232
J. Med. Chem. 2022, 65, 9011−9033

Table 2. Properties with a Significant Correlation with the Observed Inhibitory Effect on *T. brucei* for Compounds in the Merged Series Calculated with QikProp[43a]

compound	QPlogKp	QPlogPo/w	QPlogKhsa	cohesive index	CIQPlogS	%inhibition of *T. brucei* at 10 μM ± SD	EC_{50} *T. brucei* [μM] ± SD	CC_{50} [μM]	selectivity index
5a	−6.74	−1.16	0.05	0.04	−4.53	30 ± 8	N.D.	N.D.	N.D.
5b	−6.48	−1.32	**0.43**	0.04	−6.35	23 ± 4	N.D.	N.D.	N.D.
5c	−5.18	2.02	0.04	0.03	−5.32	57 ± 10	N.D.	N.D.	N.D.
5d	**-3.91**	2.19	0.07	**0.02**	−5.43	78 ± 3	0.66 ± 0.48	25 < CC_{50} < 50	38
5e	−4.60	**3.36**	−1.23	**0.02**	−3.20	100 ± 0	4.53 ± 0.42	12.5 < CC_{50} < 25	3
5f	−5.16	2.09	−1.14	**0.02**	−3.44	100 ± 0	1.30 ± 0.05	12.5 < CC_{50} < 25	10
pentamidine	N.D.	N.D.	N.D.	N.D.	N.D.	N.D.	0.0019 ± 0.0005	10	5263

[a]The properties are defined as in Table 1. Values shown in bold face are within 90% of the previously determined top value or exceeded the previously obtained range for the reference compounds and compounds in the N10-, PABA-, and Tail-modified series; see Table 1. The activity against the *T. brucei brucei* Lister 427 bloodstream form at a 10 μM compound concentration (%inhibition) is given. For the most promising compounds, **5d−5f**, in addition, measured EC_{50} values, CC_{50} interval estimations, and selectivity indices are reported and compared to pentamidine, a reference compound with activity against *T. brucei*. EC_{50} represents the arithmetic average of at least two independent measurements done in triplicate. CC_{50} estimation was done by at least three independent cytotoxicity assessments on THP-1-derived macrophages by a colorimetric MTT (3-(4,5-dimethylthiazol-2-yl)-2,5-diphenyl tetrazolium bromide) assay, as previously reported.[45] The selectivity index is determined as the CC_{50} or lower CC_{50} interval estimation divided by EC_{50}. N.D.: Not determined.

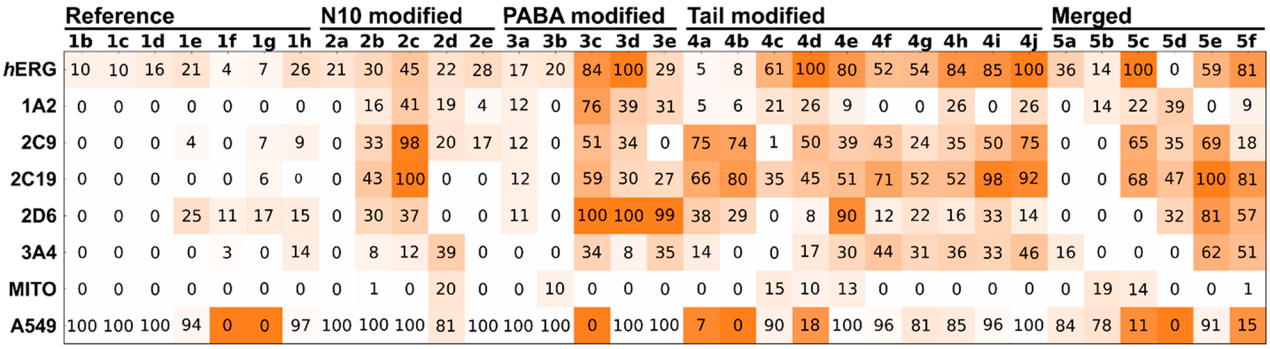

Figure 12. Heatmap representation of the liability assessment results for all the compounds studied. Inhibition of *h*ERG as well as five CYP isoforms (1A2, 2C9, 2C19, 2D6, and 3A4), mitochondrial toxicity (MITO), and growth inhibition of A549 cells were determined at 10 μM. The data are represented as percentages on a color scale from white (desired) to orange (undesired) with values reported in the map. For the inhibitory activities against *h*ERG, CYP isoforms, and mitochondrial toxicity, white = 0% and orange = 100% inhibition/toxicity, while for A549 cell growth inhibition, white = 100% and orange = 0% growth. The values are reported in Tables S8 and S9.

activity for the altered scaffold of parent **4i** in the parasite enzymes in **5e** and **5f**. Thus, combined N10 and tail modifications allowed for the species-specific optimization of the target inhibition profile.

Compounds **5d−5f** show an improved percentage of *T. brucei* inhibition at 10 μM, in line with their selection for synthesis being motivated by altered marker properties (Figure 10B). For these compounds, EC_{50} values were determined; see Table 2. Indeed, the more lipophilic compounds were found to have low micromolar EC_{50}s against *T. brucei brucei*, with **5d** being the best (EC_{50} 0.66 ± 0.48 μM), and they have SIs of 3−38 based on their cytotoxicity on THP-1-derived macrophages.

Bulky Compounds with Hydrophobic Substituents Often Display Liabilities. Potential liabilities were assessed by determining the inhibition of the *h*ERG potassium channel as well as five isoforms of CYP450 (1A2, 2C9, 2C19, 2D6, and 3A4), cytotoxicity against A459 cells (human lung adenocarcinoma epithelial cell line), and mitochondrial toxiticity against 786-O cells (renal carcinoma cell line) for all compounds at a concentration of 10 μM. The results are shown in Figure 12. Further, the compounds were assessed for and passed a check for being pan-assay interference compounds (PAINS).

The reference compounds and the N10 series mostly exhibit a safe profile. In contrast, aromatic modifications to the compound tail region, for instance in **3d**, **4j**, and **5f** (PABA, Tail, and Merged series, respectively) were associated with notable *h*ERG liabilities. Increasing the hydrophobicity of the compounds further led to liabilities against some CYP isoforms, in particular, 2C9 and 2C19. The shortened tails of **3c** and **3d** resulted in a strong effect on CYP isoform 2D6. Finally, several of the bulky, more hydrophobic compounds resulted in a cytostatic or cytotoxic effect on A549 cells. Overall, the liability assessment suggests that increasing hydrophobicity is associated with greater compound liabilities.

In line with these observations, two of the best inhibitors of *T. brucei* bloodstream forms, **5e** and **5f**, show 54 and 81% *h*ERG inhibition, respectively. **5e**, and in many cases **5f**, affects various CYP isoforms. Finally, **5f** is cytostatic with A549 cell growth reduced to 15%, and **5d** shows cytotoxicity, effectively completely inhibiting cell growth. Thus, the most active inhibitors of *T. brucei* bloodstream forms were found to suffer from liabilities associated with their greater hydrophobicity and would require careful optimization of their cellular specificity.

https://doi.org/10.1021/acs.jmedchem.2c00232
J. Med. Chem. 2022, 65, 9011−9033

CONCLUSIONS

We applied a multitarget-based approach to the development of novel therapies for HAT and leishmaniasis, in which we focused on pteridine-based inhibitors of *L. major* and *T. brucei* PTR1 and DHFR, and successfully designed the first known apparent picomolar inhibitors of *Tb*PTR1. While *Lm*PTR1/*Lm*DHFR inhibition was previously explored for this compound class,[26] we here demonstrated the potential of pteridine-based inhibitors against *Tb*PTR1 and *Tb*DHFR. We solved a crystal structure of the reference compound **1b** bound to *Tb*PTR1 to confirm the overlap in observed binding modes between *Lm*PTR1 and *Tb*PTR1 and the preference of the methotrexate inhibitor-like bound orientation in *Tb*PTR1. Guided by our detailed comparative study of on- and off-targets in the parasitic and human folate pathway,[31] crystal structures of reference compounds, and enzymatic evaluation of published reference pteridines,[26,30] we designed 26 new pteridine derivatives that mostly have improved activity and selectivity. For their synthesis, we made use of an advanced MW-assisted protocol to improve the reaction yield of the pteroid step with reduced reaction time compared to previous synthetic procedures.[33] Further determination of the crystal structures of complexes and computational docking enabled us to obtain a complete characterization of the binding modes of the pteridines to their molecular targets and supported the derivation of a SAR. The compounds were also tested against the human off-targets hDHFR and hTS. While they were sometimes only modestly selective for the parasitic DHFR variant, many showed 1000-fold and higher selectivities for PTR1 over the off-targets and thus, the novel PTR1 inhibitors can overall be considered selective for the parasite proteins.

While many compounds exhibited excellent inhibitory activity at the target level, they were often only modest inhibitors of *T. brucei brucei* bloodstream forms and inactive toward *L. infantum* intracellular amastigotes *in vitro*. We found that increased lipophilicity correlated with improved inhibitory effects on *T. brucei*. We were able to prioritize compounds for synthesis from a designed combinatorial *in silico* library by using predicted ADMET-related properties, which suggested a likely improvement of the trypanocidal effect. In this way, we identified three improved compounds, **5d**, **5e** and **5f**, with low micromolar inhibition of *T. brucei brucei* (EC_{50} 0.66−4.53 μM).

The modulated on-target/off-target activities and selectivities of the above compounds showed that specific combinations of the N10 and tail modifications allow a fine-tuning of the target inhibition profile for enzymes of specific parasite species. Furthermore, the strategy employed here of combining property prediction correlation with multitarget-based compound design was found to be a useful approach to discovering antiparasitic agents, even when the antiparasitic data are available only as a percentage of inhibition determined at a single compound concentration. We also note that the presence of high folate concentrations in the HMI-9 medium used in the parasite assays may have resulted in underestimated antiparasitic activity due to competition between folic acid and folate-analogue inhibitors of DHFR. However, our main aim in this work was to identify potent PTR1 inhibitors with antiparasitic activity that are capable of targeting multiple enzymes. In future work, these compounds can be progressed to more in-depth mechanistic studies in various parasite and mice models. Further, integration of transport-related considerations in the design,[31] or using, for instance, structurally related scaffolds reported in the literature, which show inhibition of the *Leishmania* parasite, and a similar property-based correlation concept to that presented here, may help to overcome the current limitations of the pteridine-based compounds as inhibitors of intracellular parasites. Our data show that, overall, optimization for increased lipophilicity leads to more potent pteridine-based *T. brucei* inhibitors. However, increased lipophilicity can also introduce compound liabilities, e.g. for *h*ERG and CYPs. Strategies to avoid these, for instance by making use of a similar property-based optimization strategy, should thus be incorporated in future design efforts.

EXPERIMENTAL PROCEDURES

General Synthesis Information. Reagent grade chemicals and solvents were purchased from commercial suppliers and used without further purification. Reactions were monitored by TLC on silica gel plates (Kieselgel 60, F254, Merck) and visualized using UV light, cerium ammonium sulfate, or alkaline $KMnO_4$ aqueous solution. Solvents are abbreviated as follows: tetrahydrofuran (THF), ethyl ether (Et_2O), dimethyl sulfoxide (DMSO), dimethylacetamide (DMA), ethyl acetate (EtOAc), dichloromethane (DCM), dimethylformamide (DMF), methanol (MeOH), and acetonitrile (ACN). The structures of the isolated compounds were confirmed by NMR spectroscopy and mass spectrometry. NMR spectra were recorded on Bruker 400 and 600 spectrometers with ^1H at 400.134−600 MHz and ^{13}C at 100.62−151 MHz and are given in the Supporting Information. The purity of all synthesized compounds was determined by elemental analyses performed on a PerkinElmer 240C instrument and liquid chromatography−mass spectrometry (LC−MS) on UHPLC−HRMS (Agilent 6500 QTOF mass spectrometer) under electrospray ionization mode, with 4800 V of ion voltage at Centro Interdipartimentale Grandi Strumenti, CIGS UniMoRe). The purity of the reported compounds is >95%. Exact monoisotopic masses are reported in the Supporting information along with the melting point intervals of all compounds, which were measured on a Stuart SMP3 instrument.

*General Synthetic Procedure A: Reductive Alkylation of Amines Using Nitriles (**32**, **33**, **51**, **74**).* After two vacuum/H_2 cycles to remove air from the reaction tube, the stirred mixture of the amine (1.0 equiv), Pd\C catalyst (10 wt % of the amine), the respective RCN (5.0 equiv), and NH_4OAc (1.0 equiv) in MeOH (5.0 mL) was hydrogenated under ambient pressure (balloon) at room temperature (rt) for the appropriate time (24−36 h). The reaction mixture was filtrated using Celite cake before the filtrate was concentrated under reduced pressure. The residue was partitioned between Et_2O (10 mL) and water (10 mL). The aqueous phase was extracted thrice with Et_2O (10 mL), and the combined organic phases were washed with brine (10 mL), dried with anhydrous Na_2SO_4, filtered, and concentrated under reduced pressure to yield the amines without further purification.

*General Synthetic Procedure B: Amide Coupling Reaction for the Synthesis of **27**, **28**, **40**−**49**, **52**−**54**, **56**, **57**, **71**, **72**, **75**.* Carboxylic acid compounds (1 equiv), EDC·HCl (1.1 equiv), and HOBt (0.1 equiv) were added to a dried round-bottomed flask and dissolved in DMF dry under N_2. The reaction mixture was cooled down to 0 °C and stirred for 30 min before it was added to the respective amine (1 equiv) with/without TEA (2−3 equiv). After mixing overnight at rt, the mixture was washed 1× with saturated $NaHCO_3$, 1× with H_2O, and 1× with brine. The washed organic mixture was then dried with Na_2SO_4, concentrated *in vacuo*, and purified using column chromatography (SiO_2, eluent: Cy/EtOAc or DCM/MeOH or DCM/EtOAc/MeOH) to give the desired amide.

*General Synthetic Procedure C: MW Alkylation **1b,c**, **2a**−**e**, **3a**−**c**, **4a**−**j**, **5a**−**f**.* To a suspension of amine intermediates (1 equiv) in DMA (3 mL) in a microwave Biotage vial, **29** (1.2 equiv), K_2CO_3 (3 equiv), and KI (0.1 equiv) were added. The vial was sealed and heated by microwave irradiation in a Biotage Initiator+ microwave at 60 °C for 20 min (30′ for compounds **3c**, **4d**, and **5d**), before cooling to rt and diluting with water (20 mL). The precipitate was then collected by filtration and dried before the final compound was purified by fractional crystallization from methanol, DCM, and Et_2O.

https://doi.org/10.1021/acs.jmedchem.2c00232
J. Med. Chem. 2022, 65, 9011−9033

*General Synthetic Procedure D: S_NAr for the Preparation of 4-Substituted Benzaldehyde (**63**–**65**).* A mixture of substituted phenol **58**-**60** (1 equiv), 4-fluorobenzaldehyde (1 equiv), and K_2CO_3 (3 equiv) in DMF (10 mL) was refluxed for 16–18 h under nitrogen. After cooling, the solution was concentrated *in vacuo* to give a crude residue, which was purified by crystallization in 1 M $NaHCO_3$. The obtained crystal was washed with H_2O to obtain the desired benzaldehyde derivatives.

*General Synthetic Procedure E: Preparation of Primary Amines from 4-Substituted Benzaldehyde (**66**–**68**).* A solution of carbonyl (aldehyde) compounds **66**–**68** (1 equiv) and hydroxylammonium chloride (1.2 equiv) in ethanol (30 mL) was stirred for 1 h at rt. Subsequently, 12 M hydrochloric acid (4 equiv) and zinc dust (2.5 equiv) were slowly added to the solution and left to stir at rt for 15 min. To the resulting slurry, a solution of ammonia (30%, 14 mL) and sodium hydroxide (6 M, 30 mL) was added dropwise, and the mixture was stirred at rt for another 15 min. Then, the resulting solution was extracted with DCM, dried over anhydrous Na_2SO_4, and filtered. The solvent was removed under vacuum to give the amines without further purification.

Protein Expression and Purification. Recombinant *Tb*PTR1, *Lm*PTR1, *Tb*DHFR-TS, *Lm*DHFR-TS, hDHFR, and hTS were expressed and purified according to previously reported procedures.[26,45,46]

Crystallization of *Tb*PTR1 and *Lm*PTR1. Well-ordered monoclinic crystals of histidine-tagged *Tb*PTR1 were obtained by the vapor diffusion hanging drop technique at rt.[47] Drops were prepared by mixing equal volumes of protein and precipitant solution (2–2.5 M sodium acetate and 0.1 M sodium citrate pH 5) according to a previously described procedure.[45] The *Tb*PTR1–cofactor–inhibitor ternary complexes were obtained by the soaking technique. The compounds, solubilized in DMSO, were diluted in the cryoprotectant solution (30% vol/vol glycerol added to the precipitant solution) to a final concentration of 2–4 mM (keeping the DMSO concentration below 10% vol/vol). Crystals were then transferred in the resulting soaking/cryoprotectant solution and flash frozen in liquid nitrogen after 8–24 h of exposure.

Crystals of *Lm*PTR1 were prepared as described elsewhere.[38] The *Lm*PTR1–cofactor–**2e** ternary complex was obtained by the soaking technique via the addition of 2 mM compound (solubilized in DMSO, without exceeding the 10% drop volume) directly into the crystallization drop. After 5 h, crystals were transferred to the cryoprotectant solution and flash frozen in liquid nitrogen.

Data Collection, Structure Solution, and Refinement. X-ray crystallographic data were collected using synchrotron radiation at the Diamond Light Source (DLS, Didcot, United Kingdom) beamlines I04-1 and I03 equipped with a Dectris Pilatus 6M-F and a Pilatus3 6 M detector, respectively. Reflections were integrated using MOSFLM and scaled with Scala (CCP4 suite).[48–52] Data collection and processing statistics are reported in Table S2. The crystals of *Tb*PTR1 and *Lm*PTR1 belonged to the primitive monoclinic space group $P2_1$ and the primitive orthorhombic space group $P2_12_12_1$, respectively. Both had a functional enzyme tetramer in the asymmetric unit. The structures were solved by molecular replacement using MOLREP and either a *Tb*PTR1 (PDB-ID 5jdc) or a *Lm*PTR1 tetramer (PDB-ID 5l4n) as the searching model (all nonprotein atoms were excluded).[38,45,53] Models were refined using REFMAC5 (CCP4 suite).[54] Visual inspection and manual rebuilding of missing atoms was performed using Coot.[55,56] Water molecules were added with the automated standard procedures implemented in the software ARP/wARP and checked with Coot.[57] In the higher-resolution complexes of *Tb*PTR1 with compounds **2a** and **2e**, all atoms were refined anisotropically in the final refinement cycles, and hydrogen atoms were added in the calculated positions. The occupancies of exogenous ligands were individually adjusted to values resulting in atomic displacement parameters comparable to those of surrounding protein atoms in fully occupied sites. The final models were checked with Coot and Procheck.[58] Statistics for data refinement are reported in Table S3. Figures were generated using CCP4mg.[59] Coordinates and structure factors were deposited in the Protein Data Bank under the PDB-IDs 6rx5 (*Tb*PTR1-NADPH/$NADP^+$-**1b**), 6rx0 (*Tb*PTR1-NADPH/$NADP^+$-**2a**), 6rx6 (*Tb*PTR1-NADPH/$NADP^+$-**2e**), and 6rxc (*Lm*PTR1-NADPH/$NADP^+$-**2e**).

***Tb*PTR1, *Tb*DHFR, *Lm*PTR1, *Lm*DHFR, hDHFR, and hTS Target/Off-Target Enzyme Assays.** *In vitro* assays for *Tb*PTR1 and *Lm*PTR1 were based on the coupled assay reported by Shanks et al.[60] The assay nonenzymatically links the reduction of cytochrome c (*Cc*) with the reduction of dihydrobiopterin to tetrahydrobiopterin, catalyzed by PTR1. The formation of reduced *Cc* (Fe^{2+}) results in a signal increase in the photometric readout at 550 nm wavelength. *Tb*PTR1 and *Lm*PTR1 assays were performed in a buffer containing 20 nM sodium citrate (pH 6.0) in a well-plate-based format as previously reported.[45] *Lm*DHFR, *Tb*DHFR, hDHFR, and hTS activities were assessed spectrophotometrically according to published procedures.[61,62] Each inhibitory compound was assayed at 11 different concentrations in triplicate, and IC_{50} values were calculated as described in the SI.

Computational Preparation of Pteridine Compounds and Protein Receptors and SiteMap Calculation of DHFR Pocket Volumes. The 3D structures of the reference and designed compounds were generated from SMILES strings and optimized with the OPLS_2005 force field using LigPrep of Maestro (Schrödinger, LLC) as described previously, except that tautomers were created for the pH range 5.0–8.0, and both N1-deprotonated and N1-protonated tautomers were considered for every compound.[45,63–66] In addition, all different substituents to the N10 position, PABA modifications, and compound tail alterations present in compounds **1b**–**4j** were combined in all possible permutations *in silico* in a "merged" series and prepared similarly.

All receptors were prepared in the presence of MTX (from the following PDB-IDs for *Tb*PTR1: 2c7v, *Lm*PTR1: 1e7w, TbDHFR and *Lm*DHFR: 3cl9 and hDHFR: 1u72) to improve the interactions of binding site residues and the conserved water molecules with the pteridine core. Receptor preparation was following published procedures with minor modifications.[45,63,64,67–69] For the *Lm*PTR1 (PDB-ID 1e92) and *Tb*PTR1 (PDB-ID 2x9g) receptors, an energy minimization with a harmonic restraint of 25 kcal mol^{-1} $Å^{-2}$ on heavy atoms and no restraint on hydrogens was performed until the heavy atom RMSD relative to the previous minimization step was less than 0.30 Å.[70] For the *Tb*DHFR receptor, PDB-ID 3rg9 was used; for *Lm*DHFR, our previously published homology model based on a *Tc*DHFR-TS template (PDB-ID 3inv) was chosen.[31] For off-target docking, we used the hDHFR structure 1u72. For PTR1, we also considered the previously described set of conserved water molecules identified by a WatCH clustering approach.[45,67] Further, using WatCH, we identified conserved water sites in hDHFR as described in the SI.[67] Except for the parasite DHFR variants, where the identification of a conserved water set was not possible, all receptors were prepared both with the identified set of conserved structural waters and without explicit water molecules. Grid preparation was done as described before for *Lm*PTR1 and *Tb*PTR1[45] with the following grid centers and rotatable groups: (i) *Lm*PTR1: center Phe113, rotatable OH in Ser111, Thr184, Tyr191, Tyr194, Thr195, Tyr283, and $NADP^+$ ribose; (ii) *Tb*PTR1: center Phe97, rotatable OH/SH in Ser95, Cys168, Tyr174, and $NADP^+$ ribose; (iii) *Lm*DHFR: center Phe31, rotatable OH/SH in Thr35, Thr36, Ser61, Cys130, Tyr137, Thr155, and $NADP^+$ ribose; (iv) *Tb*DHFR: center Phe58, rotatable OH in Thr46, Thr62, Thr86, Ser89, Ser98, Tyr166, Thr184, and $NADP^+$ ribose; and (v) hDHFR: center Phe34, rotatable OH in Thr38, Thr39, Ser59, Tyr121, and $NADP^+$ ribose.

The volumes of the binding pockets of *Tb*DHFR (PDB-ID 3rg9), hDHFR (1u72), and the *Lm*DHFR homology model were computed with Schrödinger SiteMap[63,71,72] as described in the SI.

Computational Docking Studies. Docking studies were performed using a rigid receptor in Glide standard precision (SP) and extra precision (XP) modes and employing the Induced Fit (IF) protocol to allow for refinement of binding site residues.[63,73–79] For rigid receptor docking, van der Waals radii scaling of ligand atoms and settings for sampling, addition of Epik state penalties to the docking score, rewarding of intramolecular hydrogen bonds, and enhancement of the planarity of conjugated π-groups were chosen as described

https://doi.org/10.1021/acs.jmedchem.2c00232
J. Med. Chem. 2022, 65, 9011–9033

previously,[45] but a total of 50 poses per ligand were subjected to postdocking energy minimization. For the *in silico* library, we used SP docking with a constraint on all heavy atoms of the pteridine core to match the orientation of MTX in the corresponding protein receptor with a tolerance of 1 Å.

In addition, since some compounds showed major variation in substituent size when compared to the starting scaffold and explicit water molecules are treated as frozen in the standard SP/XP docking, additional studies allowing protein side chain and water reorganization in response to ligand binding were performed using the standard protocol for the IF workflow implemented in Maestro. The planarity of conjugated π-groups was enhanced, and a Prime refinement was performed for residue side chains within 5 Å of ligand atoms. XP redocking was done as previously described, yielding up to 20 receptor−ligand complexes per compound.[45]

The validation of the docking protocol is presented in the SI.

Computational Property Prediction, Pan-assay Interference Compounds (PAINS), and Correlation Analysis with Antiparasitic Data. Physicochemical descriptors and parameters related to ADMET were computed for all prepared compounds using QikProp (Schrödinger).[43] Pearson correlations (R), R^2 values, and two-tailed P-values for each property with the measured percentage of inhibition of *T. brucei* at the 10 μM compound concentration were computed using SciPy and Python scripts written for the purpose. Only properties with a P-value equal to or below the statistical significance level $\alpha = 0.05$ were considered further. To ensure robustness, a resampling analysis was performed by leaving every compound out once before recomputing the correlations. Properties with $R > 0.40$ or < -0.40 and a P-value $\leq \alpha$ in >50% of the resampling correlation analyses were considered to be the most robust markers for the optimization for antiparasitic effect. These properties were employed to prioritize compounds for synthesis as part of the Merged series; for details, see the SI and Figure S9.

In addition, a multivariate correlation coefficient between parasite target protein inhibition and antiparasitic activity was computed; for details, see the SI.

Finally, all synthesized compounds were checked for PAINS filters A, B, and C, undesirable substructure moieties, covalent inhibition, and compliance with the rule-of-five with the FAF-Drugs4 Web server (https://fafdrugs4.rpbs.univ-paris-diderot.fr) by inputing SMILES strings for the compounds.[80]

***In Vitro* Biological Evaluation against *T. brucei* and *L. infantum* Intramacrophage Amastigotes.** The efficacy against *T. brucei brucei* Lister 427 bloodstream forms was evaluated in a modified resazurin-based assay as previously described.[81] Cells were grown at 37 °C and 5% CO_2 in a complete HMI-9 medium supplemented with 10% fetal calf serum (FCS) and 100 UI/mL of penicillin/streptomycin. The HMI-9 medium was selected due to its high folic acid content (9 μM), resulting in efficient parasite growth and enabling process standardization.[82] The same medium was used in our previous experiments and allowed maintenance of similar relative folate metabolism levels between models studied in high- and low-throughput systems, namely, between *Trypanosoma* cells and mouse models, and between mouse models and human plasma.[83,84] Cultures were then diluted to a cell density of 2×10^6 /mL. For the assay, compounds were prepared in 10 mM DMSO and diluted in HMI-9 to a 40 μM solution (0.4% DMSO). The assay solution was further used to perform serial dilutions (1:2) in a 96-well plate. Mid log bloodstream forms (100 μL) were added in complete HMI-9 medium at a final cell density of 1×10^4 /mL in a well volume of 200 μL after compound addition, leading to a maximum DMSO concentration of 0.2%. Following incubation for 72 h at 37 °C and 5% CO_2, 20 μL of 0.5 mM resazurin solution was added, and plates were further incubated for 4 h under similar conditions. Fluorescence was then measured using a Synergy 2 multimode reader (BioTek) at 540 and 620 nm excitation and emission wavelength, respectively. The efficacy of compounds against *L. infantum* intracellular amastigotes was determined according to Sereno et al. with slight modifications described in detail in the SI.[85]

Liability Assays. The *h*ERG cardiotoxicity assay was performed using the Invitrogen Predictor *h*ERG fluorescence polarization (FP) assay. A membrane fraction containing *h*ERG (Predictor *h*ERG membrane) was used together with a red fluorescent high-affinity ligand of the *h*ERG channel (Predictor *h*ERG Tracer Red). Displacement of the latter from *h*ERG by binding of the test compound can be determined in an FP-based format.[45]

Cytochrome P450 (CYP450) assays against isoforms 1A2, 2C9, 2C19, 2D6, and 3A4 were performed using the Promega P450-Glo assay platform. Microsomal preparations of cytochrome P450s from baculovirus-infected insect cells were used. In this assay, light is generated when a CYP450 enzyme acts on its substrate and a decrease thereof was indicative of inhibitory effects of the tested compound on the respective isoform.[45]

For monitoring mitochondrial toxicity caused by the test compounds in the 786-O cell line, uptake of MitoTracker Red (chloromethyl-X-rosamine) combined with high content imaging was used. Cells were maintained in Roswell Park Memorial Institute (RPMI)-1640 medium containing 2 mM glutamine, FCS (10% v/v), streptomycin (100 μg/mL), and penicillin G (100 U/mL).[45]

The cytotoxicity assay against A549 cells was performed using the CellTiter-Glo assay from Promega. The number of viable cells present is directly proportional to the cellular ATP content, which is detected. The A549 cells were obtained from DSMZ (German Collection of Microorganisms and Cell Cultures, Braunschweig, Germany) and grown in Dulbecco's modified Eagle medium (DMEM) with FCS (10% v/v), streptomycin (100 μg/mL), and penicillin G (100 U/mL).[45]

■ ASSOCIATED CONTENT

Supporting Information

The Supporting Information is available free of charge at https://pubs.acs.org/doi/10.1021/acs.jmedchem.2c00232.

Supplemental figures S1−9, supplemental tables S1−12, supplemental experimental procedures and compound characterization, NMR spectra of compounds (PDF)

SMILES and activities of compounds (CSV)

Accession Codes

Crystal structures described in this paper are available in the Protein Data Bank with identifiers: 6rx5 (*Tb*PTR1-NADPH/$NADP^+$-**1b**), 6rx0 (*Tb*PTR1-NADPH/$NADP^+$-**2a**), 6rx6 (*Tb*PTR1-NADPH/$NADP^+$-**2e**), 6rxc (*Lm*PTR1-NADPH/$NADP^+$-**2e**).

■ AUTHOR INFORMATION

Corresponding Authors

Maria P. Costi − *Department of Life Sciences, University of Modena and Reggio Emilia, 41125 Modena, Italy;* orcid.org/0000-0002-0443-5402; Email: mariapaola.costi@unimore.it

Alberto Venturelli − *Tydock Pharma srl, 41126 Modena, Italy; Department of Life Sciences, University of Modena and Reggio Emilia, 41125 Modena, Italy*; Email: alberto.venturelli@unimore.it

Rebecca C. Wade − *Molecular and Cellular Modeling Group, Heidelberg Institute for Theoretical Studies (HITS), D-69118 Heidelberg, Germany; Faculty of Biosciences, Center for Molecular Biology (ZMBH), DKFZ-ZMBH Alliance, and Interdisciplinary Center for Scientific Computing (IWR), Heidelberg University, D-69120 Heidelberg, Germany;* orcid.org/0000-0001-5951-8670; Email: rebecca.wade@h-its.org

Authors

Ina Pöhner − *Molecular and Cellular Modeling Group, Heidelberg Institute for Theoretical Studies (HITS), D-69118 Heidelberg, Germany; Faculty of Biosciences, Heidelberg University, D-69120 Heidelberg, Germany;* Present Address: School of Pharmacy, University of Eastern

Finland, 70211 Kuopio, Finland. (I.P.); orcid.org/0000-0002-2801-8902
Antonio Quotadamo − *Tydock Pharma srl, 41126 Modena, Italy; Clinical and Experimental Medicine PhD Program, University of Modena and Reggio Emilia, 41121 Modena, Italy*
Joanna Panecka-Hofman − *Molecular and Cellular Modeling Group, Heidelberg Institute for Theoretical Studies (HITS), D-69118 Heidelberg, Germany; Faculty of Physics, University of Warsaw, 02-093 Warsaw, Poland;* orcid.org/0000-0003-4149-9090
Rosaria Luciani − *Department of Life Sciences, University of Modena and Reggio Emilia, 41125 Modena, Italy*
Matteo Santucci − *Department of Life Sciences, University of Modena and Reggio Emilia, 41125 Modena, Italy*
Pasquale Linciano − *Department of Life Sciences, University of Modena and Reggio Emilia, 41125 Modena, Italy*
Giacomo Landi − *Department of Biotechnology, Chemistry and Pharmacy, University of Siena, 53100 Siena, Italy*
Flavio Di Pisa − *Department of Biotechnology, Chemistry and Pharmacy, University of Siena, 53100 Siena, Italy*
Lucia Dello Iacono − *Department of Biotechnology, Chemistry and Pharmacy, University of Siena, 53100 Siena, Italy*
Cecilia Pozzi − *Department of Biotechnology, Chemistry and Pharmacy, University of Siena, 53100 Siena, Italy;* orcid.org/0000-0003-2574-3911
Stefano Mangani − *Department of Biotechnology, Chemistry and Pharmacy, University of Siena, 53100 Siena, Italy;* orcid.org/0000-0003-4824-7478
Sheraz Gul − *Fraunhofer Institute for Translational Medicine and Pharmacology ITMP, Discovery Research ScreeningPort, D-22525 Hamburg, Germany*
Gesa Witt − *Fraunhofer Institute for Translational Medicine and Pharmacology ITMP, Discovery Research ScreeningPort, D-22525 Hamburg, Germany*
Bernhard Ellinger − *Fraunhofer Institute for Translational Medicine and Pharmacology ITMP, Discovery Research ScreeningPort, D-22525 Hamburg, Germany*
Maria Kuzikov − *Fraunhofer Institute for Translational Medicine and Pharmacology ITMP, Discovery Research ScreeningPort, D-22525 Hamburg, Germany;* orcid.org/0000-0001-8771-1865
Nuno Santarem − *Instituto de Investigação e Inovação em Saúde, Institute for Molecular and Cell Biology, Universidade do Porto, 4200-135 Porto, Portugal*
Anabela Cordeiro-da-Silva − *Instituto de Investigação e Inovação em Saúde, Institute for Molecular and Cell Biology, Universidade do Porto, 4200-135 Porto, Portugal; Faculty of Pharmacy, University of Porto, 4050-313 Porto, Portugal*

Complete contact information is available at: https://pubs.acs.org/10.1021/acs.jmedchem.2c00232

Author Contributions

[§§]I.P. and A.Q. are joint first authors.

Author Contributions

Conceptualization, M.P.C., A.V., R.C.W.; computational methodology and investigation, I.P., J.P.-H.; chemical synthesis methodology and investigation, A.Q.; enzyme assay methodology and investigation, R.L., M.S., P.L.; crystallography methodology and investigation, G.L., F.D.P., L.D.I., C.P.; ADMET methodology and investigation, S.G., G.W., B.E., M.K.; parasite assay methodology and investigation, N.S.; writing − original draft, I.P., writing − review & editing, I.P., J.P.-H., M.P.C., R.C.W.; supervision, S.M., A.C.S., M.P.C., A.V., R.C.W.

Notes

The authors declare no competing financial interest.
Additional supplementary data are freely available at https://doi.org/10.15490/fairdomhub.1.investigation.417.1: QikProp prediction results for synthesized and *in silico* pteridines and corresponding SOP. PAINS filtering results, Python modules for correlating QikProp data with experimental activities and for computing a multiple correlation between target and parasite inhibition. Compound library construction data and SOP, prepared docking receptors (PDB) with SOP, all Glide XP rigid-body docking results as PDB files of the receptor−ligand complexes and SOP as well as selected discussed induced fit docking results and corresponding SOP.

■ ACKNOWLEDGMENTS

This work has received funding from the European Union's Seventh Framework Programme for research, technological development, and demonstration under grant agreement no. 603240 (NMTrypI, New Medicines for Trypanosomatidic Infections, https://fp7-nmtrypi.eu/). We thank Prof. Antonio Carta, University of Sassari, for providing the reference compounds **1d−1h**. I.P., J.P.-H., and R.C.W. gratefully acknowledge the support of the Klaus Tschira Foundation. J.P.-H. acknowledges support from the Polish National Science Centre (grant no. 2016/21/D/NZ1/02806), the BIOMS program at the Interdisciplinary Center for Scientific Computing (IWR), Heidelberg University, and the Interdisciplinary Centre for Mathematical and Computational Modelling (ICM), University of Warsaw (grant no. G70-13, GB70-11, GA73-25).

■ ABBREVIATIONS USED

DHFR, dihydrofolate reductase; HAT, human African trypanosomiasis; MTX, methotrexate; NTDs, neglected tropical diseases; PABA, *para*-amino benzoic acid; PAINS, pan-assay interference compounds; PTR1, pteridine reductase 1; SI, selectivity index; TS, thymidylate synthase

■ REFERENCES

(1) Neglected tropical diseases. https://www.who.int/neglected_diseases/en/ (accessed May 2020).
(2) The WHO Strategic and Technical Advisory Group for Neglected Tropical Diseases (WHO STAG). https://www.who.int/publications/i/item/9789240015098.
(3) Barrett, M. P.; Burchmore, R. J. S.; Stich, A.; Lazzari, J. O.; Frasch, A. C.; Cazzulo, J. J.; Krishna, S. The trypanosomiases. *Lancet.* **2003**, *362*, 1469−1480.
(4) Blum, J.; Schmid, C.; Burri, C. Clinical aspects of 2541 patients with second stage human African trypanosomiasis. *Acta Trop.* **2006**, *97*, 55−64.
(5) Stuart, K.; Brun, R.; Croft, S.; Fairlamb, A.; Gürtler, R. E.; McKerrow, J.; Reed, S.; Tarleton, R. Kinetoplastids: related protozoan pathogens, different diseases. *J. Clin. Invest.* **2008**, *118*, 1301−1310.
(6) Cunningham, A. C. Parasitic adaptive mechanisms in infection by *Leishmania*. *Exp. Mol. Pathol.* **2002**, *72*, 132−141.
(7) Herwaldt, B. L. Leishmaniasis. *Lancet.* **1999**, *354*, 1191−1199.
(8) Castillo, E.; Dea-Ayuela, M. A.; Bolás-Fernández, F.; Rangel, M.; González-Rosende, M. E. The kinetoplastid chemotherapy revisited: current drugs, recent advances and future perspectives. *Curr. Med. Chem.* **2010**, *17*, 4027−4051.
(9) Machado-Silva, A.; Goulart Guimarães, P. P.; Pereira Tavares, C. A.; Sinisterra, R. D. New perspectives for leishmaniasis chemotherapy

over current anti-leishmanial drugs: a patent landscape. *Expert Opin. Ther. Pat.* **2015**, *25*, 247−260.
(10) Gilbert, I. H. Drug discovery for neglected diseases: molecular target-based and phenotypic approaches. *J. Med. Chem.* **2013**, *56*, 7719−7726.
(11) Müller, J.; Hemphill, A. Drug target identification in protozoan parasites. *Expert Opin. Drug Discovery* **2016**, *11*, 815−824.
(12) Borsari, C.; Quotadamo, A.; Ferrari, S.; Venturelli, A.; Cordeiro-da-Silva, A.; Santarem, N.; Costi, M. P. Chapter Two - Scaffolds and biological targets avenue to fight against drug resistance in leishmaniasis. *Annu. Rep. Med. Chem.* **2018**, *51*, 39−95.
(13) Shuvalov, O.; Petukhov, A.; Daks, A.; Fedorova, O.; Vasileva, E.; Barlev, N. A. One-carbon metabolism and nucleotide biosynthesis as attractive targets for anticancer therapy. *Oncotarget* **2017**, *8*, 23955−23977.
(14) Anderson, A. C.; Wright, D. L. Antifolate agents: a patent review (2010 - 2013). *Expert Opin. Ther. Pat.* **2014**, *24*, 687−697.
(15) Hawser, S.; Lociuro, S.; Islam, K. Dihydrofolate reductase inhibitors as antibacterial agents. *Biochem. Pharmacol.* **2006**, *71*, 941−948.
(16) Yuthavong, Y.; Yuvaniyama, J.; Chitnumsub, P.; Vanichtanankul, J.; Chusacultanachai, S.; Tarnchompoo, B.; Vilaivan, T.; Kamchonwongpaisan, S. Malarial (*Plasmodium falciparum*) dihydrofolate reductase-thymidylate synthase: structural basis for antifolate resistance and development of effective inhibitors. *Parasitology* **2005**, *130*, 249−259.
(17) Christensen, K. E.; MacKenzie, R. E. Mitochondrial one-carbon metabolism is adapted to the specific needs of yeast, plants and mammals. *Bioessays* **2006**, *28*, 595−605.
(18) Cullia, G.; Tamborini, L.; Conti, P.; De Micheli, C.; Pinto, A. Folates in *Trypanosoma brucei*: Achievements and opportunities. *ChemMedChem.* **2018**, *13*, 2150−2158.
(19) Bello, A. R.; Nare, B.; Freedman, D.; Hardy, L.; Beverley, S. M. PTR1: A reductase mediating salvage of oxidized pteridines and methotrexate resistance in the protozoan parasite *Leishmania major*. *Proc. Natl. Acad. Sci. U. S. A.* **1994**, *91*, 11442−11446.
(20) Dawson, A.; Gibellini, F.; Sienkiewicz, N.; Tulloch, L. B.; Fyfe, P. K.; McLuskey, K.; Fairlamb, A. H.; Hunter, W. N. Structure and reactivity of *Trypanosoma brucei* pteridine reductase: inhibition by the archetypal antifolate methotrexate. *Mol. Microbiol.* **2006**, *61*, 1457−1468.
(21) Vickers, T. J.; Beverley, S. M. Folate metabolic pathways in *Leishmania*. *Essays Biochem.* **2011**, *51*, 63−80.
(22) Ong, H. B.; Sienkiewicz, N.; Wyllie, S.; Fairlamb, A. H. Dissecting the metabolic roles of pteridine reductase 1 in *Trypanosoma brucei* and *Leishmania major*. *J. Biol. Chem.* **2011**, *286*, 10429−10438.
(23) Sienkiewicz, N.; Ong, H. B.; Fairlamb, A. H. *Trypanosoma brucei* pteridine reductase 1 is essential for survival in vitro and for virulence in mice. *Mol. Microbiol.* **2010**, *77*, 658−671.
(24) Mpamhanga, C. P.; Spinks, D.; Tulloch, L. B.; Shanks, E. J.; Robinson, D. A.; Collie, I. T.; Fairlamb, A. H.; Wyatt, P. G.; Frearson, J. A.; Hunter, W. N.; Gilbert, I. H.; Brenk, R. One scaffold, three binding modes: Novel and selective pteridine reductase 1 inhibitors derived from fragment hits discovered by virtual screening. *J. Med. Chem.* **2009**, *52*, 4454−4465.
(25) Spinks, D.; Ong, H. B.; Mpamhanga, C. P.; Shanks, E. J.; Robinson, D. A.; Collie, I. T.; Read, K. D.; Frearson, J. A.; Wyatt, P. G.; Brenk, R.; Fairlamb, A. H.; Gilbert, I. H. Design, synthesis and biological evaluation of novel inhibitors of *Trypanosoma brucei* pteridine reductase 1. *ChemMedChem.* **2011**, *6*, 302−308.
(26) Cavazzuti, A.; Paglietti, G.; Hunter, W. N.; Gamarro, F.; Piras, S.; Loriga, M.; Allecca, S.; Corona, P.; McLuskey, K.; Tulloch, L.; Gibellini, F.; Ferrari, S.; Costi, M. P. Discovery of potent pteridine reductase inhibitors to guide antiparasite drug development. *Proc. Natl. Acad. Sci. U. S. A.* **2008**, *105*, 1448−1453.
(27) Ivanetich, K. M.; Santi, D. V. Bifunctional thymidylate synthase-dihydrofolate reductase in protozoa. *FASEB J.* **1990**, *4*, 1591−1597.
(28) Schormann, N.; Senkovich, O.; Walker, K.; Wright, D. L.; Anderson, A. C.; Rosowsky, A.; Ananthan, S.; Shinkre, B.; Velu, S.; Chattopadhyay, D. Structure-based approach to pharmacophore identification, *in silico* screening, and three-dimensional quantitative structure-activity relationship studies for inhibitors of *Trypanosoma cruzi* dihydrofolate reductase function. *Proteins* **2008**, *73*, 889−901.
(29) Schormann, N.; Velu, S. E.; Murugesan, S.; Senkovich, O.; Walker, K.; Chenna, B. C.; Shinkre, B.; Desai, A.; Chattopadhyay, D. Synthesis and characterization of potent inhibitors of *Trypanosoma cruzi* dihydrofolate reductase. *Bioorg. Med. Chem.* **2010**, *18*, 4056−4066.
(30) Corona, P.; Gibellini, F.; Cavalli, A.; Saxena, P.; Carta, A.; Loriga, M.; Luciani, R.; Paglietti, G.; Guerrieri, D.; Nerini, E.; Gupta, S.; Hannaert, V.; Michels, P. A. M.; Ferrari, S.; Costi, P. M. Structure-based selectivity optimization of piperidine-pteridine derivatives as potent *Leishmania* pteridine reductase inhibitors. *J. Med. Chem.* **2012**, *55*, 8318−8329.
(31) Panecka-Hofman, J.; Pöhner, I.; Spyrakis, F.; Zeppelin, T.; Di Pisa, F.; Dello Iacono, L.; Bonucci, A.; Quotadamo, A.; Venturelli, A.; Mangani, S.; Costi, M. P.; Wade, R. C. Comparative mapping of on-targets and off-targets for the discovery of anti-trypanosomatid folate pathway inhibitors. *Biochim. Biophys. Acta, Gen. Subj.* **2017**, *1861*, 3215−3230.
(32) Tulloch, L. B.; Martini, V. P.; Iulek, J.; Huggan, J. K.; Lee, J. H.; Gibson, C. L.; Smith, T. K.; Suckling, C. J.; Hunter, W. N. Structure-based design of pteridine reductase inhibitors targeting African sleeping sickness and the leishmaniases. *J. Med. Chem.* **2010**, *53*, 221−229.
(33) Quotadamo, A.; Linciano, P.; Costi, M. P.; Venturelli, A. Optimization of *N*-alkylation in the synthesis of methotrexate and pteridine-based derivatives under microwave-irradiation. *ChemistrySelect* **2019**, *4*, 4429−4433.
(34) Sajiki, H.; Ikawa, T.; Hirota, K. Reductive and catalytic monoalkylation of primary amines using nitriles as an alkylating reagent. *Org. Lett.* **2004**, *6*, 4977−4980.
(35) Ikawa, T.; Fujita, Y.; Mizusaki, T.; Betsuin, S.; Takamatsu, H.; Maegawa, T.; Monguchi, Y.; Sajiki, H. Selective N-alkylation of amines using nitriles under hydrogenation conditions: facile synthesis of secondary and tertiary amines. *Org. Biomol. Chem.* **2012**, *10*, 293−304.
(36) Ayedi, M. A.; Le Bigot, Y.; Ammar, H.; Abid, S.; El Gharbi, R.; Delmas, M. Synthesis of primary amines by one-pot reductive amination of aldehydes. *Synth. Commun.* **2013**, *43*, 2127−2133.
(37) Gourley, D. G.; Schüttelkopf, A. W.; Leonard, G. A.; Luba, J.; Hardy, L. W.; Beverley, S. M.; Hunter, W. N. Pteridine reductase mechanism correlates pterin metabolism with drug resistance in trypanosomatid parasites. *Nat. Struct. Biol.* **2001**, *8*, 521−525.
(38) Di Pisa, F.; Landi, G.; Dello Iacono, L.; Pozzi, C.; Borsari, C.; Ferrari, S.; Santucci, M.; Santarem, N.; Cordeiro-da-Silva, A.; Moraes, C. B.; Alcantara, L. M.; Fontana, V.; Freitas-Junior, L. H.; Gul, S.; Kuzikov, M.; Behrens, B.; Pöhner, I.; Wade, R. C.; Costi, M. P.; Mangani, S. Chroman-4-one derivatives targeting pteridine reductase 1 and showing anti-parasitic activity. *Molecules* **2017**, *22*, 426.
(39) Lloyd, M. D. High-Throughput Screening for the Discovery of Enzyme Inhibitors. *J. Med. Chem.* **2020**, *63*, 10742−10772.
(40) Holdgate, G.; Meek, T.; Grimley, R. Mechanistic enzymology in drug discovery: a fresh perspective. *Nat. Rev. Drug Discovery* **2018**, *17*, 115−132.
(41) Synold, T. W.; Willits, E. M.; Barredo, J. C. Role of folylpolyglutamate synthetase (FPGS) in antifolate chemotherapy; a biochemical and clinical update. *Leuk. Lymphoma* **1996**, *21*, 9−15.
(42) Gibson, M. W.; Dewar, S.; Ong, H. B.; Sienkiewicz, N.; Fairlamb, A. H. *Trypanosoma brucei* DHFR-TS revisited: characterisation of a bifunctional and highly unstable recombinant dihydrofolate reductase-thymidylate synthase. *PLoS Negl. Trop. Dis.* **2016**, *10*, e0004714.
(43) *Schrödinger Release 2015-4: QikProp v4.6*, Schrödinger, LLC: New York, NY, 2015.
(44) Jorgensen, W. L.; Duffy, E. M. Prediction of drug solubility from Monte Carlo simulations. *Bioorg. Med. Chem. Lett.* **2000**, *10*, 1155−1158.
(45) Borsari, C.; Luciani, R.; Pozzi, C.; Poehner, I.; Henrich, S.; Trande, M.; Cordeiro-da-Silva, A.; Santarem, N.; Baptista, C.; Tait, A.; Di Pisa, F.; Dello Iacono, L.; Landi, G.; Gul, S.; Wolf, M.; Kuzikov, M.;

https://doi.org/10.1021/acs.jmedchem.2c00232
J. Med. Chem. 2022, 65, 9011−9033

Ellinger, B.; Reinshagen, J.; Witt, G.; Gribbon, P.; Kohler, M.; Keminer, O.; Behrens, B.; Costantino, L.; Tejera Nevado, P.; Bifeld, E.; Eick, J.; Clos, J.; Torrado, J.; Jiménez-Antón, M. D.; Corral, M. J.; Alunda, J. M.; Pellati, F.; Wade, R. C.; Ferrari, S.; Mangani, S.; Costi, M. P. Profiling of flavonol derivatives for the development of antitrypanosomatidic drugs. *J. Med. Chem.* **2016**, *59*, 7598−7616.

(46) Cardinale, D.; Guaitoli, G.; Tondi, D.; Luciani, R.; Henrich, S.; Salo-Ahen, O. M.; Ferrari, S.; Marverti, G.; Guerrieri, D.; Ligabue, A.; Frassineti, C.; Pozzi, C.; Mangani, S.; Fessas, D.; Guerrini, R.; Ponterini, G.; Wade, R. C.; Costi, M. P. Protein-protein interface-binding peptides inhibit the cancer therapy target human thymidylate synthase. *Proc. Natl. Acad. Sci. U. S. A.* **2011**, *108*, E542−E549.

(47) Benvenuti, M.; Mangani, S. Crystallization of soluble proteins in vapor diffusion for X-ray crystallography. *Nat. Protoc.* **2007**, *2*, 1633−1651.

(48) Battye, T. G. G.; Kontogiannis, L.; Johnson, O.; Powell, H. R.; Leslie, A. G. W. iMOSFLM: a new graphical interface for diffraction-image processing with MOSFLM. *Acta Crystallogr. D Biol Crystallogr* **2011**, *67*, 271−281.

(49) Powell, H. R.; Johnson, O.; Leslie, A. G. W. Autoindexing diffraction images with *iMosflm*. *Acta Crystallogr. D Biol Crystallogr* **2013**, *69*, 1195−1203.

(50) Evans, P. Scaling and assessment of data quality. *Acta Crystallogr. D Biol Crystallogr* **2006**, *62*, 72−82.

(51) Evans, P. An introduction to data reduction: space-group determination, scaling and intensity statistics. *Acta Crystallogr. D Biol Crystallogr.* **2011**, *67*, 282−292.

(52) CCP4. The CCP4 suite: programs for protein crystallography. *Acta Crystallogr. D Biol Crystallogr.* **1994**, *50*, 760−763.

(53) Vagin, A.; Teplyakov, A. Molecular replacement with *MOLREP*. *Acta Crystallogr. D Biol Crystallogr.* **2010**, *66*, 22−25.

(54) Murshudov, G. N.; Skubák, P.; Lebedev, A. A.; Pannu, N. S.; Steiner, R. A.; Nicholls, R. A.; Winn, M. D.; Long, F.; Vagin, A. A. *REFMAC5* for the refinement of macromolecular crystal structures. *Acta Crystallogr. D Biol Crystallogr* **2011**, *67*, 355−367.

(55) Emsley, P.; Cowtan, K. *Coot*: model-building tools for molecular graphics. *Acta Crystallogr. D Biol Crystallogr* **2004**, *60*, 2126−2132.

(56) Emsley, P.; Lohkamp, B.; Scott, W. G.; Cowtan, K. Features and development of *Coot*. *Acta Crystallogr. D Biol Crystallogr* **2010**, *66*, 486−501.

(57) Langer, G. G.; Cohen, S. X.; Lamzin, V. S.; Perrakis, A. Automated macromolecular model building for X-ray crystallography using ARP/wARP version 7. *Nat. Protoc.* **2008**, *3*, 1171−1179.

(58) Laskowski, R. A.; MacArthur, M. W.; Thornton, J. M. Validation of protein models derived from experiment. *Curr. Opin. Struct. Biol.* **1998**, *8*, 631−639.

(59) Potterton, L.; McNicholas, S.; Krissinel, E.; Gruber, J.; Cowtan, K.; Emsley, P.; Murshudov, G. N.; Cohen, S.; Perrakis, A.; Noble, M. Developments in the *CCP4* molecular-graphics project. *Acta Crystallogr. D Biol Crystallogr* **2004**, *60*, 2288−2294.

(60) Shanks, E. J.; Ong, H. B.; Robinson, D. A.; Thompson, S.; Sienkiewicz, N.; Fairlamb, A. H.; Frearson, J. A. Development and validation of a cytochrome *c*-coupled assay for pteridine reductase 1 and dihydrofolate reductase. *Anal. Biochem.* **2010**, *396*, 194−203.

(61) Ferrari, S.; Morandi, F.; Motiejunas, D.; Nerini, E.; Henrich, S.; Luciani, R.; Venturelli, A.; Lazzari, S.; Calò, S.; Gupta, S.; Hannaert, V.; Michels, P. A. M.; Wade, R. C.; Costi, M. P. Virtual screening identification of nonfolate compounds, including a CNS drug, as antiparasitic agents inhibiting pteridine reductase. *J. Med. Chem.* **2011**, *54*, 211−221.

(62) Tan, X.; Huang, S.; Ratnam, M.; Thompson, P. D.; Freisheim, J. H. The importance of loop region residues 40−46 in human dihydrofolate reductase as revealed by site-directed mutagenesis. *J. Biol. Chem.* **1990**, *265*, 8027−8032.

(63) *Schrödinger Release 2015-4: LigPrep v3.6; Epik v3.4; Protein Preparation Wizard (PrepWizard); SiteMap v3.7; Glide v6.9; Induced Fit Docking Protocol; Prime v4.2*, Schrödinger, LLC: New York, NY, 2015.

(64) Linciano, P.; Dawson, A.; Pöhner, I.; Costa, D. M.; Sá, M. S.; Cordeiro-da-Silva, A.; Luciani, R.; Gul, S.; Witt, G.; Ellinger, B.; Kuzikov, M.; Gribbon, P.; Reinshagen, J.; Wolf, M.; Behrens, B.; Hannaert, V.; Michels, P. A. M.; Nerini, E.; Pozzi, C.; Di Pisa, F.; Landi, G.; Santarem, N.; Ferrari, S.; Saxena, P.; Lazzari, S.; Cannazza, G.; Freitas-Junior, L. H.; Moraes, C. B.; Pascoalino, B. S.; Alcântara, L. M.; Bertolacini, C. P.; Fontana, V.; Wittig, U.; Müller, W.; Wade, R. C.; Hunter, W. N.; Mangani, S.; Costantino, L.; Costi, M. P. Exploiting the 2-Amino-1,3,4-thiadiazole scaffold to inhibit *Trypanosoma brucei* pteridine reductase in support of early-stage drug discovery. *ACS Omega* **2017**, *2*, 5666−5683.

(65) Shelley, J. C.; Cholleti, A.; Frye, L. L.; Greenwood, J. R.; Timlin, M. R.; Uchimaya, M. Epik: a software program for pK_a prediction and protonation state generation for drug-like molecules. *J. Comput. Aided Mol. Des.* **2007**, *21*, 681−691.

(66) Greenwood, J. R.; Calkins, D.; Sullivan, A. P.; Shelley, J. C. Towards the comprehensive, rapid, and accurate prediction of the favorable tautomeric states of drug-like molecules in aqueous solution. *J. Comput. Aided Mol. Des.* **2010**, *24*, 591−604.

(67) Sanschagrin, P. C.; Kuhn, L. A. Cluster analysis of consensus water sites in thrombin and trypsin shows conservation between serine proteases and contributions to ligand specificity. *Protein Sci.* **1998**, *7*, 2054−2064.

(68) Madhavi Sastry, G.; Adzhigirey, M.; Day, T.; Annabhimoju, R.; Sherman, W. Protein and ligand preparation: parameters, protocols, and influence on virtual screening enrichments. *J. Comput. Aided Mol. Des.* **2013**, *27*, 221−234.

(69) Li, H.; Robertson, A. D.; Jensen, J. H. Very fast empirical prediction and rationalization of protein pKa values. *Proteins* **2005**, *61*, 704−721.

(70) Banks, J. L.; Beard, H. S.; Cao, Y.; Cho, A. E.; Damm, W.; Farid, R.; Felts, A. K.; Halgren, T. A.; Mainz, D. T.; Maple, J. R.; Murphy, R.; Philipp, D. M.; Repasky, M. P.; Zhang, L. Y.; Berne, B. J.; Friesner, R. A.; Gallicchio, E.; Levy, R. M. Integrated Modeling Program, Applied Chemical Theory (IMPACT). *J. Comput. Chem.* **2005**, *26*, 1752−1780.

(71) Halgren, T. New method for fast and accurate binding-site identification and analysis. *Chem. Biol. Drug Des.* **2007**, *69*, 146−148.

(72) Halgren, T. A. Identifying and characterizing binding sites and assessing druggability. *J. Chem. Inf. Model.* **2009**, *49*, 377−389.

(73) Friesner, R. A.; Banks, J. L.; Murphy, R. B.; Halgren, T. A.; Klicic, J. J.; Mainz, D. T.; Repasky, M. P.; Knoll, E. H.; Shelley, M.; Perry, J. K.; Shaw, D. E.; Francis, P.; Shenkin, P. S. Glide: a new approach for rapid, accurate docking and scoring. 1. Method and assessment of docking accuracy. *J. Med. Chem.* **2004**, *47*, 1739−1749.

(74) Halgren, T. A.; Murphy, R. B.; Friesner, R. A.; Beard, H. S.; Frye, L. L.; Pollard, W. T.; Banks, J. L. Glide: a new approach for rapid, accurate docking and scoring. 2. Enrichment factors in database screening. *J. Med. Chem.* **2004**, *47*, 1750−1759.

(75) Friesner, R. A.; Murphy, R. B.; Repasky, M. P.; Frye, L. L.; Greenwood, J. R.; Halgren, T. A.; Sanschagrin, P. C.; Mainz, D. T. Extra Precision Glide: Docking and scoring incorporating a model of hydrophobic wnclosure for protein-ligand complexes. *J. Med. Chem.* **2006**, *49*, 6177−6196.

(76) Sherman, W.; Beard, H. S.; Farid, R. Use of an induced fit receptor structure in virtual screening. *Chem. Biol. Drug Des.* **2006**, *67*, 83−84.

(77) Sherman, W.; Day, T.; Jacobson, M. P.; Friesner, R. A.; Farid, R. Novel procedure for modeling ligand/receptor induced fit effects. *J. Med. Chem.* **2006**, *49*, 534−553.

(78) Jacobson, M. P.; Pincus, D. L.; Rapp, C. S.; Day, T. J. F.; Honig, B.; Shaw, D. E.; Friesner, R. A. A hierarchical approach to all-atom protein loop prediction. *Proteins* **2004**, *55*, 351−367.

(79) Jacobson, M. P.; Friesner, R. A.; Xiang, Z.; Honig, B. On the role of the crystal environment in determining protein side-chain conformations. *J. Mol. Biol.* **2002**, *320*, 597−608.

(80) Lagorce, D.; Sperandio, O.; Baell, J. B.; Miteva, M. A.; Villoutreix, B. O. FAF-Drugs3: a web server for compound property calculation and chemical library design. *Nucleic Acids Res.* **2015**, *43*, W200−W207.

(81) Bowling, T.; Mercer, L.; Don, R.; Jacobs, R.; Nare, B. Application of a resazurin-based high-throughput screening assay for the

https://doi.org/10.1021/acs.jmedchem.2c00232
J. Med. Chem. 2022, 65, 9011−9033

identification and progression of new treatments for human African trypanosomiasis. *Int. J. Parasitol. Drugs Drug Resist.* **2012**, *2*, 262−270.
(82) Hirumi, H.; Hirumi, K. Continuous cultivation of *Trypanosoma brucei* blood stream forms in a medium containing a low concentration of serum protein without feeder cell layers. *J. Parasitol.* **1989**, *75*, 985−989.
(83) Linciano, P.; Cullia, G.; Borsari, C.; Santucci, M.; Ferrari, S.; Witt, G.; Gul, S.; Kuzikov, M.; Ellinger, B.; Santarém, N.; Cordeiro da Silva, A.; Conti, P.; Bolognesi, M. L.; Roberti, M.; Prati, F.; Bartoccini, F.; Retini, M.; Piersanti, G.; Cavalli, A.; Goldoni, L.; Bertozzi, S. M.; Bertozzi, F.; Brambilla, E.; Rizzo, V.; Piomelli, D.; Pinto, A.; Bandiera, T.; Costi, M. P. Identification of a 2,4-diaminopyrimidine scaffold targeting *Trypanosoma brucei* pteridine reductase 1 from the LIBRA compound library screening campaign. *Eur. J. Med. Chem.* **2020**, *189*, 112047.
(84) Leamon, C. P.; Reddy, J. A.; Dorton, R.; Bloomfield, A.; Emsweller, K.; Parker, N.; Westrick, E. Impact of high and low folate diets on tissue folate receptor levels and antitumor responses toward folate-drug conjugates. *J. Pharmacol. Exp. Ther.* **2008**, *327*, 918−925.
(85) Sereno, D.; Cavaleyra, M.; Zemzoumi, K.; Maquaire, S.; Ouaissi, A.; Lemesre, J. L. Axenically grown amastigotes of *Leishmania infantum* used as an in vitro model to investigate the pentavalent antimony mode of action. *Antimicrob. Agents Chemother.* **1998**, *42*, 3097−3102.

Recommended by ACS

Discovery and Optimization of Potent and Orally Available CTP Synthetase Inhibitors for Use in Treatment of Diseases Driven by Aberrant Immune Cell Proliferation

Andrew Novak, Geraint Jones, *et al.*
NOVEMBER 30, 2022
JOURNAL OF MEDICINAL CHEMISTRY
READ

Exploring the Activity Profile of TbrPDEB1 and hPDE4 Inhibitors Using Free Energy Perturbation

Lorena Zara, Iwan J. P. de Esch, *et al.*
MAY 23, 2022
ACS MEDICINAL CHEMISTRY LETTERS
READ

Optimization of Potent and Specific Trypanothione Reductase Inhibitors: A Structure-Based Drug Discovery Approach

Theo Battista, Giuseppe Campiani, *et al.*
JULY 26, 2022
ACS INFECTIOUS DISEASES
READ

Optimization of TAM16, a Benzofuran That Inhibits the Thioesterase Activity of Pks13; Evaluation toward a Preclinical Candidate for a Novel Antituberculosis Clinica...

Caroline Wilson, Paul G. Wyatt, *et al.*
DECEMBER 15, 2021
JOURNAL OF MEDICINAL CHEMISTRY
READ

Get More Suggestions >

https://doi.org/10.1021/acs.jmedchem.2c00232
J. Med. Chem. 2022, 65, 9011−9033